

The Structure of the Nucleon: Elastic Electromagnetic Form Factors

V. Punjabi¹, C.F. Perdrisat², M.K. Jones³, E.J. Brash^{3,4}, and C.E. Carlson²

¹ Norfolk State University, Norfolk, VA 23504, USA

² The College of William & Mary, Williamsburg, VA 23187, USA

³ Thomas Jefferson National Accelerator Facility, Newport News, VA 23606, USA

⁴ Christopher Newport University, Newport News, VA 23606, USA

Received: December 12, 2014/ Revised version: December 12, 2014

Abstract. Precise proton and neutron form factor measurements at Jefferson Lab, using spin observables, have recently made a tremendous contribution to unraveling of the internal structure of the nucleon. Accurate experimental measurements of the nucleon form factors are a testbed for understanding how their static properties and dynamical behavior emerge from QCD, the theory of the strong interactions between quarks. There has been enormous theoretical progresses since the publication of the Jefferson Lab proton form factor ratio data, aiming at reevaluating the picture of the nucleon. We will review the experimental and theoretical progress, such as generalized parton distributions and flavor separation, Dyson-Schwinger equations (DSEs) calculations, improvements made in lattice QCD calculations, and more.

PACS. PACS-key describing text of that key – PACS-key describing text of that key

1 Introduction

Nucleons are the building blocks of almost all ordinary matter in the universe. The challenge of understanding the nucleon's structure and dynamics has occupied a central place in nuclear physics. The nucleon (proton and neutron) electromagnetic form factors describe the spatial distributions of electric charge and current inside the nucleon, hence are intimately related to its internal structure; these form factors are among the most basic observables of the nucleon.

Quantum chromo dynamics (QCD) is the theory of the strong interaction, which is responsible for binding quarks through the exchange of gluons to form hadrons (baryons and mesons). The fundamental understanding of the nucleon form factors in terms of QCD is one of the outstanding problems in nuclear physics. Why do quarks form colorless hadrons with only two stable configurations, proton and neutron? One important step towards answering this question is to characterize the internal structure of the nucleon. High energy electron scattering provides one of the most powerful tools to investigate this structure.

Early electron scattering experiments with nuclei were motivated by a need to verify predictions of the then current models of the electromagnetic interaction of electrons with nuclei, and in particular with the proton and neutron; Rosenbluth predicted that high energy electrons would be scattered dominantly by the magnetic moment of the pro-

ton [1]. Available accelerators in the early fifties had energies smaller than 50 MeV, and provided much information on the nuclear radius of elements from Be to Pb. First clear evidence that the proton was not point like was obtained at the Stanford accelerator in the period 1953-1956, under the leadership of Robert Hofstadter. Clear demonstration that the proton has a finite size (unlike the electron?) had to wait for the availability of electron beams with higher energy, like the 550 MeV Stanford linear accelerator. In his extensive, 1956 review Hofstadter [2] discussed data for the angular distribution of the elastically scattered electrons up to 140 degrees; these data differ from the expectation for a point charge and magnetic distribution by a factor of five at the largest $q^2 = 14 \times 10^{-26} \text{ cm}^{-2} = 14 \text{ fm}^{-2}$ or $\approx 0.73 \text{ GeV}^2$. A proton radius of $0.77 \pm 0.1 \text{ fm}$ was derived from the momentum transfer squared q^2 dependence of a form factor $F^2(q^2)$ defined in terms of the charge density distribution as:

$$\rho(r) = \frac{1}{2\pi^2 r} \int F(q) \sin(qr) q dq. \quad (1)$$

In 1957 Yennie, Levy and Ravenhall [3] derived an expression for the **ep** cross section in terms of two form factors, F_1 and F_2 , following Rosenbluth's work, as:

$$\sigma(\theta) = \sigma_{NS} \left\{ F_1^2 + \frac{q^2}{4M^2} \left[2(F_1 + F_2)^2 \tan^2 \frac{\theta_e}{2} \right] \right\}, \quad (2)$$

where F_1 was introduced to represent the spread-out charge and spread-out Dirac magnetic moment. F_2 describes the

spread-out Pauli (or anomalous) magnetic moment. σ_{NS} is equal to the Mott cross section corrected for the nucleon recoil (see Eq. 8 below).

A similar change in accepted concepts occurred when the JLab data for the proton form factor ratio $\mu_p \frac{G_{Ep}}{G_{Mp}}$ from double polarization experiments, completed in 2000 up to Q^2 of 5.8 GeV², differed drastically from the form factor results obtained using the Rosenbluth separation method; here μ_p is the magnetic moment of the proton. The standard data base up to this time had been entirely defined by cross section measurements, and suggested that, for $Q^2 < \sim 10 \text{ GeV}^2$, both the electric and magnetic form factors behaved approximately like the dipole form factor:

$$G_D = \left(1 + \frac{Q^2}{0.71}\right)^{-2}, \quad (3)$$

with the four momentum transfer squared $Q^2 = -q^2 = -(\mathbf{q}^2 - \omega^2)$; \mathbf{q} the vector polarization transfer and ω the energy transfer, in units of GeV².

What the series of experiments started in 1998 in Hall A at JLab demonstrated was that the electric and magnetic form factor ratio $\mu_p \frac{G_{Ep}}{G_{Mp}}$ decreased approximately linearly with Q^2 , reaching a value of 1/3.7 times the value at $Q^2 = 0$ at the highest Q^2 investigated at that time, 5.6 GeV². Coincidentally, Rosenbluth [1] had argued in 1950, that in a combination of the spread-out electric charge produced by the pion cloud and the strongly anomalous magnetic moment of the proton, the magnetic form factor would dominate the data at large Q^2 ; fifty years later this “prediction” was verified by the JLab data. And almost 60 year after the work of ref. [2] the question of whether the proton radius is ≈ 0.877 or 0.8409 fm, a difference of 6.9 standard deviations, is being discussed intensely.

1.1 History of elastic electron scattering on the nucleon

Elastic electron proton scattering has evolved since the history making series of experiments with electron beams at the Stanford Linear Accelerator in 1956. Under the leadership of R. Hofstadter, a series of crucial results were obtained from cross section measurements [4]. Several fundamental pieces of information were established following these experiments, including the approximate $1/Q^8$ decrease of the cross section with the invariant four momentum transfer squared, Q^2 , establishing the approximate shape of the charge distribution, and a first value for the proton radius. Theoretical work evolved in parallel with these experimental “firsts”, leading to the description of the elastic electron scattering process in terms of the lowest order process, the exchange of a single virtual photon with negative invariant mass squared; this lowest order contribution, also called the Born term, was expected to be dominant because of the smallness of the electromagnetic coupling constant α_{EM} . Fundamental expressions for the hadronic current and the definition of two invariant form factors, F_1 and F_2 , later named the Dirac and Pauli

form factors, of the Born (single photon exchange) term, were issues of this period. Experimenters use preferably the Sachs form factors G_E and G_M , which are linearly related to F_1 and F_2

$$\begin{aligned} G_{E_{p,n}} &= F_{1_{p,n}} - \tau F_{2_{p,n}} \\ G_{M_{p,n}} &= F_{1_{p,n}} + F_{2_{p,n}}, \end{aligned} \quad (4)$$

The possibility of observing polarization transfer, or asymmetry, for longitudinally polarized electrons, measuring either the polarization transferred to the recoil proton, or the asymmetry if the target proton or neutron is polarized, was first discussed in a paper by Akhiezer et al [5,6]. It was to be more than 20 years before such experiments, which require a polarized electron beam, could be performed with good accuracy. Further papers on double polarization experiments followed, including Akhiezer and Rekalo [7,8], and Dombey [9]. The accidental time coincidence of the initial phase of the construction of the CEBAF accelerator at the Thomas Jefferson National Accelerator Facility (TJNAF) or JLab, in Virginia, and a paper by Arnold, Carlson and Gross [10] about double polarization experiments, lead to an intensive program of nucleon form factor experiments and a significant breakthrough in our understanding of the proton structure. A series of double-spin experiments, first for the proton and then for the neutron, followed, with conundrum changing consequences.

In the Born approximation the transferred polarization has only two components, both in the reaction plane defined by the beam and scattered electron, one along the recoil proton momentum, and the other perpendicular to it. For the proton, polarization transfer has been used most often at JLab for the proton; it requires a re-scattering of the proton to measure its polarization, and is dependent on the analyzing power of the reaction used. For the neutron, target asymmetry has now been used successfully [11] for the determination of the G_{En}/G_{Mn} ratio; this requires a polarized target of either D₂ or He³, which limits the maximum electron current that can be tolerated without significant depolarization of the target. Recent progress in the design and construction of polarized liquid ³He-target [12] indicates that future experiments on the neutron form factors should benefit of much increased beam luminosity (at Mainz and JLab). Solid polarized proton targets also reach high polarization by Dynamic Nuclear Polarization, but suffer from beam current limitations, which mitigate some of their advantage over liquid ³He target because of the absence of nuclear effects.

Among the earliest *ep* published polarization experiments, a search in 1963 at the Saclay Linear Accelerator with a beam of 950 MeV electrons, for a symmetry breaking induced recoil polarization perpendicular to the scattering plane, for unpolarized beam electrons and unpolarized target protons, may well have been the first polarization experiment ever performed. Such an effect would be due to the interference of the Born amplitude with the two-photon exchange amplitude in elastic *ep* scattering.

The asymmetry obtained in the vertical plane at $Q^2=0.61$ GeV^2 was 0.040 ± 0.027 [13].

A similar single-spin experiment in 1970 with an unpolarized 15-18 GeV electron beam at the Stanford linear accelerator, and a polarized proton target with polarization perpendicular to the reaction plane to characterize the interference of the two-photon exchange with the single photon exchange (Born) process, produced asymmetries of order 0.5% in the range of Q^2 0.38 to 0.98 GeV^2 [14].

The early nineties saw a number of double polarization experiments at NIKHEF [15] and MAMI [16,17] to determine the neutron electric form factor up to $Q^2 \sim 1$ GeV^2 . All used polarized electron beams and a polarized target, either deuterium or ^3He .

The next step was the measurement of the transverse, in plane recoil proton polarization P_t (or P_x) for longitudinally polarized electrons and unpolarized target in the mid nineties, at the Mainz Microtron (MAMI) [18,19]. This experiment measured the proton form factor ratio G_{Ep}/G_{Mp} up to Q^2 of 0.5 GeV^2 , and the results were in agreement with the dipole form factor, $G_D = (1 + \frac{Q^2}{0.71})^{-2}$.

The start in 1998 of the recoil polarization program at JLab, both for the proton and the neutron, was preceded by experiments at the BATES Linear Accelerator. For the neutron, the pioneering experiment of Madey et al. performed the first recoil polarization measurement of G_{En} at BATES at a Q^2 of 0.255 GeV^2 in 1994 [20]. For the proton the two polarization transfer components P_ℓ and P_t , and the corresponding G_{Ep}/G_{Mp} ratio were measured at Q^2 of 0.38 to 0.50 GeV^2 [21-23].

In 2000 the SAMPLE collaboration obtained the vector analyzing power for 200 MeV transversally polarized electrons for the unpolarized proton, which is parity conserving and time-reversal odd, and tests the contribution of two-photon exchange. When compared with the results of Ref. [13], such transverse effects are suppressed by the relativist boost parameter γ . A value of $A = -15.4 \pm 5.4$ ppm at $Q^2=0.1$ GeV^2 was observed in this experiment [24]. +

1.2 Dirac and Pauli form factors

The lowest order approximation for electron nucleon scattering is the single virtual photon exchange process, or Born term. The Born approximation is expected to provide a good lowest order description of elastic eN scattering (with $N = p, n$) because of the weak electro-magnetic coupling of the photon with the charge and the magnetic moment of the nucleon. The amplitude for the process is the product of the four-component leptonic and hadronic currents, ℓ_ν and \mathcal{J}_μ , and can be written as:

$$\begin{aligned} i\mathcal{M} &= \frac{-i}{q_\mu^2} \ell_\mu \mathcal{J}^\mu \\ &= \frac{-ig_{\mu\nu}}{q_\mu^2} [ie\bar{u}(k')\gamma^\nu u(k)] [-ie\bar{v}(p')\Gamma^\mu(p', p)v(p)] \end{aligned} \quad (5)$$

where k, k', p, p' are the four-momenta of the incident and scattered, electron and proton, respectively, Γ^μ contains all information of the nucleon structure, and $g_{\mu\nu}$ is the metric tensor. To insure relativistic invariance of the amplitude \mathcal{M} , Γ^μ can only contain p, p' and γ^μ , besides numbers, masses and Q^2 .

The most general form for the hadronic current for the spin $\frac{1}{2}$ -nucleon, satisfying relativistic invariance and current conservation, and including an internal structure is:

$$\mathcal{J}_{hadronic}^\mu = ie\bar{v}(p') \left[\gamma^\mu F_1(Q^2) + \frac{i\sigma^{\mu\nu}q_\nu}{2M} \kappa_j F_2(Q^2) \right] v(p) \quad (6)$$

where M is the nucleon mass, κ_j , with $j = p, n$ the anomalous magnetic moment, in units of the nuclear magneton, $\mu_N = \frac{e\hbar}{2M}$. $Q^2 = q^2 - \omega^2 = -q_\mu^2$, is the negative of the square of the invariant mass q_μ^2 of the virtual photon of negative mass squared, exchanged in the one-photon approximation of eN scattering. The Dirac and Pauli form factors, $F_1(Q^2)$ and $F_2(Q^2)$ are the only structure functions allowed in the Born term by relativistic invariance. As is now the most frequently used notation, $\kappa_j F_2$ $j = p, n$ will be written as F_{2p} and F_{2n} , respectively. In the static limit, $Q^2 = 0$, $F_{1p} = 1$, $F_{2p} = \kappa_p = 1.7928$ and $F_{1n} = 0$ and $F_{2n} = \kappa_n = -1.9130$, for the proton and neutron, respectively.

The Lab frame differential cross section for detection of the electron in elastic ep or en scattering is then:

$$\begin{aligned} \frac{d\sigma}{d\Omega_e} &= \left(\frac{d\sigma}{d\Omega} \right)_{Mott} \frac{E_e}{E_{beam}} \left(F_1^2(Q^2) \right. \\ &\quad \left. + \tau \left[F_2^2(Q^2) + 2[F_1(Q^2) + F_2(Q^2)]^2 \tan^2 \frac{\theta_e}{2} \right] \right) \end{aligned} \quad (7)$$

with $\tau = Q^2/4M_p^2$; $(\frac{d\sigma}{d\Omega})_{Mott}$ is the Mott cross section given by:

$$\left(\frac{d\sigma}{d\Omega} \right)_{Mott} = \frac{\alpha^2 \cos^2 \frac{\theta}{2}}{4E_{beam}^2 \sin^4 \frac{\theta}{2}}. \quad (8)$$

The incident electron (beam) and scattered electron energies are labeled E_{beam} and E_e , respectively. The fraction $\frac{E_e}{E_{beam}}$ in Eq. 1.2 is the recoil correction to the Mott cross section Eq. 8.

Experimental cross section data are most easily analyzed in terms of another set of form factors, the Sachs form factors G_E and G_M . The relation between G_E and G_M and F_1 and F_2 for proton and neutron are given in Eq. 4. The scattering cross section Eq. 1.2 can then be written in a much simpler form, without interference term, leading to a separation method for G_E^2 and G_M^2 known as Rosenbluth (or Longitudinal-Transverse) method, as will be seen below. Now the cross section is:

$$\frac{d\sigma}{d\Omega_e} = \left(\frac{d\sigma}{d\Omega} \right)_{Mott} \frac{E_e}{E_{beam}} \frac{1}{1 + \tau} \left(G_{Ep}^2 + \frac{\tau}{\epsilon} G_{Mp}^2 \right) \quad (9)$$

where ϵ is the polarization of the virtual photon defined as:

$$\epsilon = \frac{1}{1 + 2(1 + \tau) \tan^2 \frac{\theta_e}{2}}, \quad (10)$$

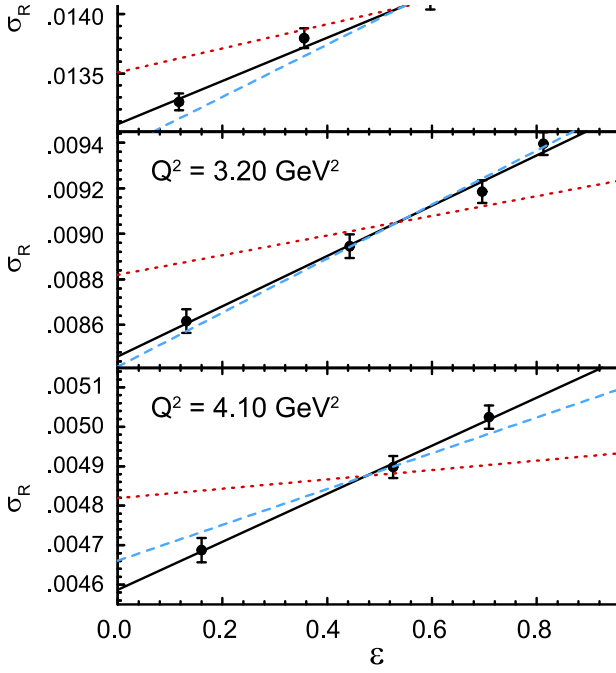


Fig. 1. Illustration of the Rosenbluth separation method to obtain separate values of G_{Ep}^2 and G_{Mp}^2 from the kinematic factor ϵ -dependence of the reduced cross section. Data from Qattan [25]

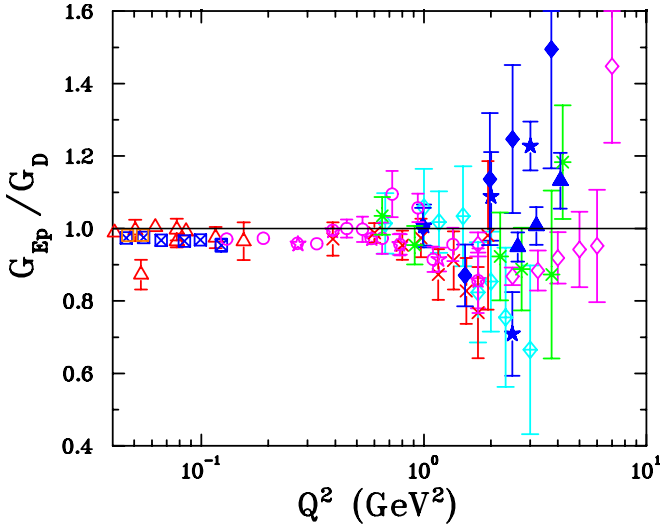


Fig. 2. Q^2 -dependence of the ratio G_{Ep}/G_D obtained by the Rosenbluth separation method. G_D is the dipole form factor. All data published after 1970 [26] are included

The modern version of the Rosenbluth separation technique takes advantage of the linear dependence in ϵ , in the reduced cross section σ_{red} , based on Eq. (9), as follows:

$$\left(\frac{d\sigma}{d\Omega}\right)_{red} = \epsilon(1+\tau)\frac{E_{beam}}{E_e} \left(\frac{d\sigma}{d\Omega}\right)_{exp} / \left(\frac{d\sigma}{d\Omega}\right)_{Mott} = \tau G_M^2 + \epsilon G_E^2, \quad (11)$$

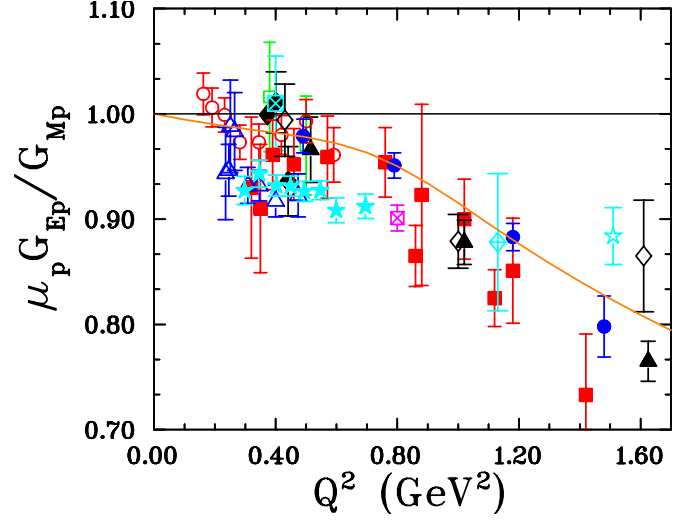


Fig. 3. Ratio $G_{Ep}G_{Mp}$ for Q^2 smaller than 1.5 GeV^2 . The inconsistency of the various experiments are highlighted here.

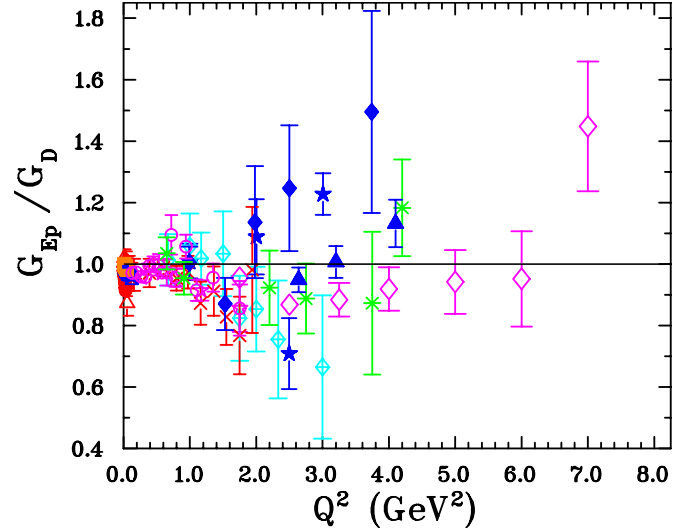


Fig. 4. Ratio $G_{Ep}G_{Mp}$ from all Rosenbluth experiments on a linear scale in Q^2 ; to be compared with the same data displayed on a log scale.

showing that the reduced cross section σ_{red} is expected to have a linear dependence on ϵ , with slope proportional to G_E^2 and intercept equal to τG_M^2 . To illustrate the method, the reduced cross section data, σ_{red} , of ref. [25] are shown in Fig. 1. The corresponding form factor ratios are shown in Fig. 3 on a background of other form factor ratios obtained from Rosenbluth separations. Also shown on this figure are the results of the first two recoil polarization experiments obtained in hall A, triangle symbols. [27–30]. The dichotomy between cross section (Rosenbluth separation) and recoil polarization results is very obvious indeed from this figure.

1.2.1 Proton Radius

In a general sense the elastic ep cross section is related to the Mott cross section for a spin $\frac{1}{2}$ electron without internal structure times the Fourier transform of the charge and/or magnetization density of the target nucleon as follows:

$$\sigma(\theta_e) = \sigma_{Mott} \times \left| \int_{volume} \rho(\mathbf{r}) \exp i \mathbf{q} \cdot \mathbf{r} d^3 \mathbf{r} \right|^2 \quad (12)$$

where $\rho(\mathbf{r})$ is either the electric- or the magnetic spacial distribution function. It follows, for the particular of the electric form factor $G_{Ep}(Q^2)$, that for short distances it can be expanded in terms of even moments of the distance $\langle r_e^{2n} \rangle$ as:

$$G_{Ep} = 1 - \frac{1}{6} Q^2 \langle r_e^2 \rangle + \frac{1}{120} Q^4 \langle r_e^4 \rangle \dots \quad (13)$$

Hence for very small distance within the nucleon, the mean-square radius of the proton can be obtained from the derivative of Eq. 13

$$\frac{dG_{Ep}}{dQ^2} = -\frac{1}{6} |left| r_e^2 |right|_{at Q^2=0} \quad (14)$$

from which follows the relation

$$\langle r_e^2 \rangle = -6 |left| \frac{dG_{Ep}}{dQ^2} |right|_{at Q^2=0}; \quad (15)$$

A similar relation holds for the magnetic radius $\langle r_m^2 \rangle$. Many electron scattering experiments have obtained values of $\langle r_e^2 \rangle$ by fitting low Q^2 cross section data [31,32]; $\langle r_m^2 \rangle$ is more difficult to obtain as its contribution to the cross section is weighted down by the factor τ (see Equ. 9).

The proton radius can also be obtained from precise measurements of the Lamb shift energies either in the hydrogen atom (Ref. [33]), or in muonic hydrogen (Ref. [34]). In both cases the 2S-2P Lamb shift is affected by the fact that the S-state wave function is maximum at the hydrogen's center, while the P-state has minimal overlap with the hydrogen nucleus. Recent measurements of the muonic Lamb shift energies at PSI have produced values of $\langle r_e^2 \rangle$ which are smaller than the mean value of all electron scattering experiments by 7σ ([35]).

1.3 Formalism of double polarization experiments

In 1968 and 1974 Akhiezer and Rekalov [5,6] discussed the interest of measuring an interference term of the form $G_E G_M$ by measuring the transverse component of the recoiling proton polarization in $ep \rightarrow ep$ at large Q^2 , to obtain G_E in the presence of a dominating G_M . In a review paper Dombey [9] emphasized the virtues of measurements with a polarized lepton beam on a polarized target to obtain polarization observables. Also much later in 1982 Arnold, Carlson and Gross [10] discussed in detail,

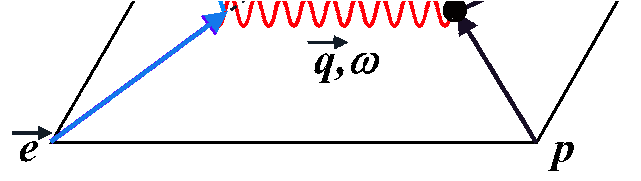


Fig. 5. Illustration of the kinematics and polarization of the recoil proton for $ep \rightarrow e'p$.

that the best way to measure the neutron and proton form factors would be to use the $^2H(e, e'n)n$ and $^1H(e, e'p)p$ reactions, respectively.

Indeed, both the recoil polarization and target asymmetry measurement methods have been used successfully to measure the proton and neutron form factors to high four momentum transfer, Q^2 , at Jefferson Lab. These methods have been used also at MIT-Bates, the Mainz Microtron (MAMI), and Nationaal Instituut voor Kernfysica en Hoge Energie Fysica (NIKHEF), to make precise proton and neutron form factor measurements at lower Q^2 . Both methods are discussed below, with benefits and drawbacks of using polarized target and focal plane polarimeter.

1.3.1 Recoil polarization method

With a longitudinally polarized electron beam and an unpolarized hydrogen target, the polarization of the incoming electron is transferred to the proton via an exchange of a virtual photon as shown in Fig. 5. For elastic ep scattering with a longitudinally polarized electron beam, the only non-zero polarization transfer observables are the longitudinal and transverse polarizations, P_ℓ and P_t . For single photon exchange, the transferred polarization can be written in terms of the Sachs form factors as:

$$\begin{aligned} I_o P_n &= 0 \\ I_o P_\ell &= h P_e \frac{(E_{beam} + E_e)}{M} \sqrt{\tau(1+\tau)} \tan^2 \frac{\theta_e}{2} G_M^2 \\ I_o P_t &= -h P_e 2 \sqrt{\tau(1+\tau)} \tan \frac{\theta_e}{2} G_E G_M \end{aligned} \quad (16)$$

where $h = \pm 1$ and P_e are the beam helicity and polarization, respectively; E_{beam} and E_e are the incident and scattered electron energies, θ_e is the electron scattering angle, and M is the mass of the proton; $I_o = G_E^2 + \frac{\tau}{\epsilon} G_M^2$, is the unpolarized cross section and $\epsilon = [1 + 2(1 + \tau) \tan^2 \frac{\theta_e}{2}]^{-1}$ is the longitudinal polarization of the virtual photon.

The ratio of G_E and G_M is then directly obtained from the ratio of the two polarizations P_t and P_ℓ components:

$$\frac{G_E}{G_M} = -\frac{P_t}{P_\ell} \frac{(E_{beam} + E_e)}{2M} \tan \left(\frac{\theta_e}{2} \right). \quad (17)$$

In the one-photon exchange process, the form factors depend only on Q^2 and a deviation from constant would indicate a mechanism beyond the Born approximation.

For each Q^2 , a single measurement of the azimuthal angular distribution of the proton scattered in a secondary target gives both the longitudinal and transverse polarizations. Thus the ratio of electric to magnetic form factors of the proton is obtained directly from a simultaneous measurement of the two recoil polarization components. The knowledge of the beam polarization and of the analyzing power of the polarimeter is not needed to extract the ratio, G_E/G_M . The kinematic factors in Eq. (17) are typically known to a precision far greater than the statistical precision of the recoil polarization components.

1.3.2 Asymmetry with polarized targets

It was discussed by Dombey [9] in a review paper in 1969 that the nucleon form factors can be extracted from the scattering of longitudinally polarized electrons off a polarized nucleon target. In the one photon exchange approximation, the elastic electron nucleon scattering cross section can be written reaction en as a sum of two parts: Σ , which corresponds to the unpolarized elastic differential cross section $d\sigma/d\Omega_e$, and a polarized part Δ , which is non-zero only if the electron beam is longitudinal polarized [36,37];

$$\sigma_h = \Sigma + h\Delta, \quad (18)$$

where h is the beam helicity, and Σ the unpolarized elastic ep cross section can be written as:

$$\Sigma = \left(\frac{d\sigma}{d\Omega} \right)_{Mott} \frac{E_e}{E_{beam}} \frac{1}{1+\tau} \left[G_E^2 + \frac{\tau}{\epsilon} G_M^2 \right]. \quad (19)$$

The polarized part of the cross section, Δ , with two terms related to the directions of the target polarization, $P(\theta^*\phi^*)$, is given by [36,37]:

$$\begin{aligned} \Delta = -2 \left(\frac{d\sigma}{d\Omega} \right)_{Mott} \frac{E_e}{E_{beam}} \tan \frac{\theta_e}{2} \sqrt{\frac{\tau}{1+\tau}} \\ \left(\sqrt{\tau[1+(1+\tau)\tan^2 \frac{\theta_e}{2}]} \cos \theta^* G_M^2 \right. \\ \left. + \sin \theta^* \cos \phi^* G_E G_M \right) \end{aligned} \quad (20)$$

where θ^* and ϕ^* are the polar and azimuthal laboratory angles of the target polarization vector with \mathbf{q} in the z direction and \mathbf{y} normal to the electron scattering plane, as shown in Figure 6.

The physical asymmetry A is then defined as

$$A = \frac{\sigma_+ - \sigma_-}{\sigma_+ + \sigma_-} = \frac{\Delta}{\Sigma}, \quad (21)$$

where σ_+ and σ_- are the cross sections for the two beam helicities.

For a longitudinally polarized beam and polarized target, the measured asymmetry, A_{meas} , is related to the physical asymmetry, A , by

$$A_{meas} = P_{beam} P_{target} A, \quad (22)$$

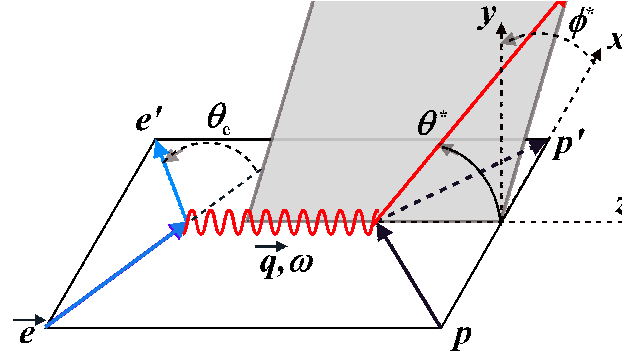


Fig. 6. Illustration of the kinematics and orientation of the target polarization P , for the reaction $en \rightarrow e'n$.

where P_{beam} and P_{target} are electron beam and target polarization, respectively, and A can be obtained using Eqs. (19) and (20),

$$\begin{aligned} A = - \frac{2\sqrt{\tau(1+\tau)} \tan \frac{\theta_e}{2}}{G_E^2 + \frac{\tau}{\epsilon} G_M^2} \left[\sin \theta^* \cos \phi^* G_E G_M \right. \\ \left. + \sqrt{\tau[1+(1+\tau)\tan^2 \frac{\theta_e}{2}]} \cos \theta^* G_M^2 \right]. \end{aligned} \quad (23)$$

From Eq. (23), it is apparent that to extract G_E , the target polarization in the laboratory frame must be perpendicular with respect to the momentum transfer vector \mathbf{q} and within the reaction plane, with $\theta^* = \pi/2$ and $\phi^* = 0^\circ$ or 180° . For these conditions, the physical asymmetry A in Eq. (23) simplifies to:

$$A_{perp} = \frac{-2\sqrt{\tau(1+\tau)} \tan \frac{\theta_e}{2} \frac{G_E}{G_M}}{\left(\frac{G_E}{G_M} \right)^2 + \frac{\tau}{\epsilon}}. \quad (24)$$

As $(G_E/G_M)^2$ is quite small, A_{perp} is approximately proportional to G_E/G_M . In practice, the second term in Eq. (23) is not strictly zero due to the finite acceptance of the detectors, but these effects are small and depend on kinematics only in first order and can be corrected for, so the ratio G_E/G_M is not affected directly.

The discussion above is only applicable to a free electron-nucleon scattering. For a quasi-elastic electron scattering from a nuclear targets, like ^2H or ^3He , corrections are required for several nuclear effects.

1.4 Two-photon exchange

In the one-photon exchange process, the form factors depend only on Q^2 and a deviation from constant would indicate a mechanism beyond the Born approximation.

In the general case, elastic ep scattering can be described by three complex amplitudes [38–41]: \tilde{G}_M , \tilde{G}_E , and \tilde{F}_3 , the first two chosen as generalizations of the Sachs electric and magnetic form factors, G_E and G_M , and the last one, \tilde{F}_3 , vanishing in case of Born approximation. The reduced cross section, σ_{red} , and the proton polarization

transfer components P_t and P_ℓ , including two-photon exchange formalism, can be written as [39]:

$$\sigma_{red} = G_M^2 + \frac{\varepsilon}{\tau} G_E^2 + 2G_M \Re \left(\delta \tilde{G}_M + \frac{\varepsilon}{M^2} \tilde{F}_3 \right) + 2 \frac{\varepsilon}{\tau} G_E \Re \left(\delta \tilde{G}_E + \frac{\nu}{M^2} \tilde{F}_3 \right) \quad (25)$$

$$\text{with} \quad \nu = \frac{s-u}{4M^2} = \sqrt{\tau(1-\tau)} \frac{1+\varepsilon}{1-\varepsilon}. \quad (26)$$

$$P_t = -\sqrt{\frac{2\varepsilon(1-\varepsilon)}{\tau}} \frac{1}{\sigma_{red}} \left(G_E G_M + G_E \Re(\delta \tilde{G}_M) + G_M \Re(\delta \tilde{G}_E + \frac{\nu}{M^2} \tilde{F}_3) \right) \quad (27)$$

$$P_\ell = \sqrt{(1-\varepsilon^2)} \frac{1}{\sigma_{red}} \left(G_M^2 + 2G_M \Re(\delta \tilde{G}_M + \frac{\varepsilon}{1+\varepsilon} \frac{\nu}{M^2} \tilde{F}_3) \right), \quad (28)$$

where:

$$\Re \tilde{G}_M(Q^2, \varepsilon) = G_M(Q^2) + \Re \delta \tilde{G}_M(Q^2, \varepsilon) \quad (29)$$

$$\Re \tilde{G}_E(Q^2, \varepsilon) = G_E(Q^2) + \Re \delta \tilde{G}_E(Q^2, \varepsilon) \quad (30)$$

Here $\tau = Q^2/4M_p^2$, and $\varepsilon = [1 + 2(1 + \tau) \tan^2 \frac{\theta_e}{2}]^{-1}$, where θ_e is the lab electron scattering angle. While the Sachs form factors depend only on Q^2 , in the general case the amplitudes depend also on ε . The reduced cross section and the transferred proton polarization components are sensitive only to the real part of the amplitudes.

In Born approximation only the first term remains in the reduced cross section, σ_{red} , and the proton polarization transfer components P_t and P_ℓ are :

$$\sigma_{red} = G_M^2 + \frac{\varepsilon}{\tau} G_E^2 \quad (31)$$

$$P_t = -\sqrt{\frac{2\varepsilon(1-\varepsilon)}{\tau}} \frac{G_E G_M}{\sigma_{red}}, \quad (32)$$

$$P_\ell = \sqrt{(1-\varepsilon^2)} \frac{G_M^2}{\sigma_{red}} \quad (33)$$

2 Recent developments; to be relocated

The experimental and theoretical situation for the nucleon form factors were reviewed extensively in the 7 years following publication of the results of the first recoil polarization experiment at Jefferson Lab [27]. Chronologically these reviews include Gao [42, 43], Hyde-Wright et al. [44], Perdrisat et al. [45] and Arrington et al. [46], Arrington et al [47], Cloet et al. [48] and Perdrisat and Punjabi [49]. At this point in time, the double-polarization method had been used up to 5.6 GeV² for the proton form factor ratio G_{Ep}/G_{Mp} ([27–29, 50], and 1.45 GeV² for G_{En}/G_{Mn} . Recent polarization experiments at JLab for G_{Mn} to a Q² of 0.6 GeV² [51] had been published, and a mix of polarization and cross section had been obtained up to 5 GeV² for G_{Mn} , the latest using the cross section ratio method, to

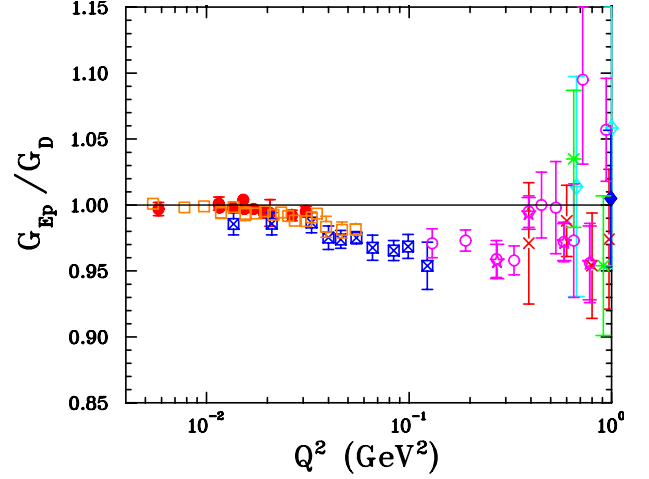


Fig. 7. Low Q^2 behavior of the G_{Rp}/G_D ratio for Q^2 smaller than 1 GeV² for Rosenbluth data, illustrating the very small deviation from a constant of this ratio for small Q^2 .

obtain G_{Mn} from the measured $\frac{d\sigma}{d\Omega} \frac{[{}^2H(e, e' n)_{QE}]}{d\sigma \frac{[{}^2H(e, e' p)_{QE}]}$ ratio [52, 53].

The principal revelation coming out of the first G_{Ep}/G_{Mp} experiment using recoil polarization was the systematic decrease of this ratio with increasing Q^2 . There existed data from the 1970's which suggested a similar behavior, although they were limited to Q^2 smaller than 3 GeV², and had large uncertainties. Interestingly, at that time, models based on vector meson dominance (VMD) [54–57] were predicting a rapid decrease of the ratio G_{Ep}/G_D , reaching a value of 0.5 at Q^2 of 4 GeV/c. In the same period, a first paper from the Stanford group [26] suggested a drastically different Q^2 dependence of the same ratio, G_{Ep}/G_{Mp} , with values reaching 1.35 \pm 0.3 at $Q^2=3.6$ GeV² (verify these numbers). The complete set of experimental results derived from cross section measurements is shown in Fig. 3 and 8. It includes the most recent JLab results of [58, 25].

Since the last review paper was published, considerable theoretical work was performed. Some of the original models discussed in the 1970's, in particular the original Vector Dominance (VMD), as well as the Constituent Quark (CQM) models were revisited, made relativistic, then more or less left the front row, with the exception of Lomon [59], Bijker [60] and others.

The proton form factors were originally introduced in non-relativistic scattering, as the three-dimensional Fourier transform of the charge density [4, 61]. However the proton recoil implies that the electron is interacting with a moving charge distribution. Already for $Q^2=0.25$ GeV², the recoil proton relativistic boost factor γ is 1.1, corresponding to $v/c = 0.41$. The argument that form factors are Fourier transforms of nucleon density in the Breit frame was abandoned, as this frame's velocity in the Lab frame is different for every Q^2 .

The proton in its ground state is not necessarily spherically symmetric, but can show a typical multipole shape,

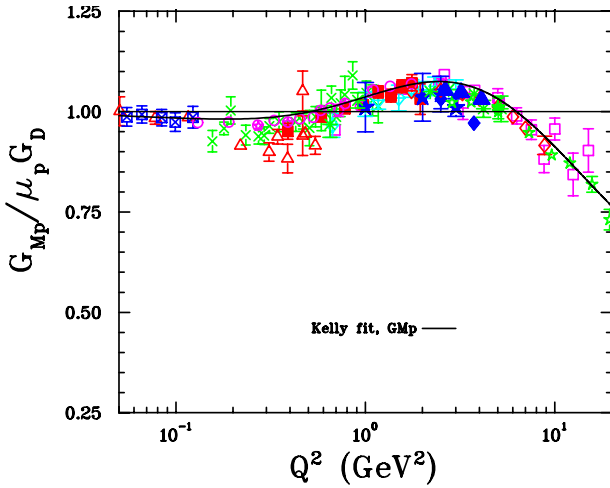


Fig. 8. Rosenbluth values of $G_{Mp}/\mu_p G_D$ including all published data, for comparison with Fig. 1.

when referred to the spin direction of one of its quarks (constituents) relative to the nucleon spin orientation [62].

The wave front or infinite momentum frame densities are invariant, two-dimensional transverse charge and magnetization distribution, and are drastically different from the non-relativistic ones [62,63].

Elastic ep scattering in the 1 to 10 GeV^2 range of 4-momentum squared transfer is the domain of non-perturbative quantum chromodynamics (QCD); as a consequence of Dynamical Chiral Symmetry Breaking, valence quarks acquire a mass of order $M_p/3$ in the infrared limit. [64,48]

Scaling as a consequence of Perturbative QCD may have visible consequences even in the non-perturbative domain [65]

The di-quark structure of the nucleon has observable consequences [66]

The mass of the dressed quarks originates from the QCD vacuum; it results from accretion of quark-antiquark pairs from decaying gluons spontaneously emerging from the vacuum [48].

Assuming isospin symmetry one can obtain flavor separated dressed quark form factors from simple linear relations between the Dirac and Pauli form factors. The dressed up and down quarks have significantly different form factors [48,67–71].

A zero crossing of G_{Ep} , if and when observed, would provide information on the dressed-quark mass function [38].

Nucleon form factors determine the parameters of the valence quark GPDs; these can be used to obtain corresponding valence quark densities [38].

The available data suggest that the isovector electric form factor (G_{Ep} - G_{En}) has a zero near $Q^2 \approx 4.3 \text{ GeV}^2$; this feature can be predicted in lattice calculations, from the connected diagram only. [38].

Soft Collinear Effective Theory (SCET), Kivel and Vanderhaeghen(2013) for two-photon exchange [41].

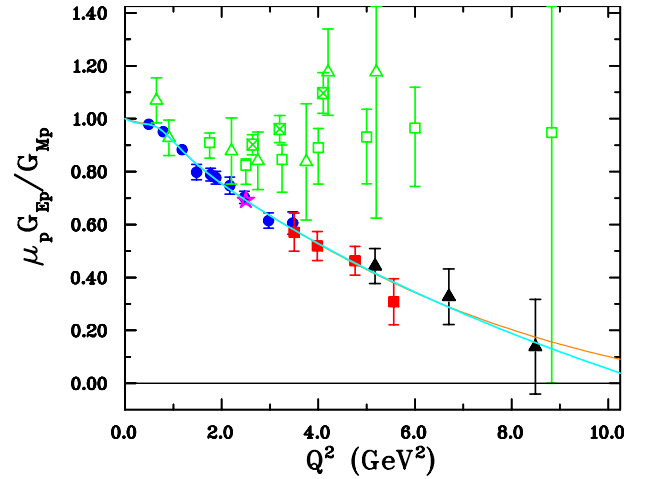


Fig. 9. All data for the ratio G_{Ep}/G_{Mp} obtained from the three large Q^2 recoil polarization experiments at JLab. Both curves are Kelly-type polynomial fits. The orange curve is a 7 parameter fit constrained with $1/Q^2$ asymptotic behavior. The azul curve a 6 parameter fits with constant asymptotic behavior.

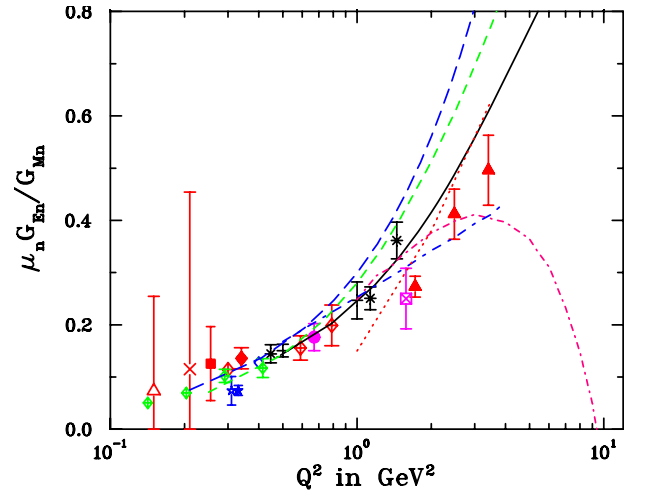


Fig. 10. The complete data base for G_{En}/G_{Mn} from double polarization experiments. Asymmetry with polarized D2 target: [15,72–74], asymmetry with polarized ^3He target: [75–81, 11,82], recoil polarization with D2 target [20,16,17,83–85]

3 G_{En} ; to be relocated

This in preparation for the neutron section, in particular fig with $\mu_n G_{En}/G_{Mn}$. Nov. 3/14.

4 More Figures

5 Asymptotic behavior

In the pQCD approach proposed by Brodsky and collaborators[88,89], the interaction is described as a convolution of a hard scattering amplitude and a baryon distribution amplitude. Up to leading order in $1/Q^2$, the magnetic

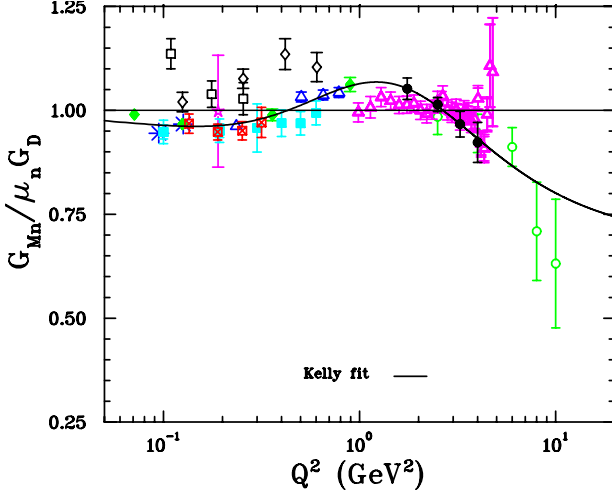


Fig. 11. The complete data base for $G_{Mn}/\mu_n G_D$. May compare with the equivalent figure for $G_{Mp}/\mu_p G_D$.

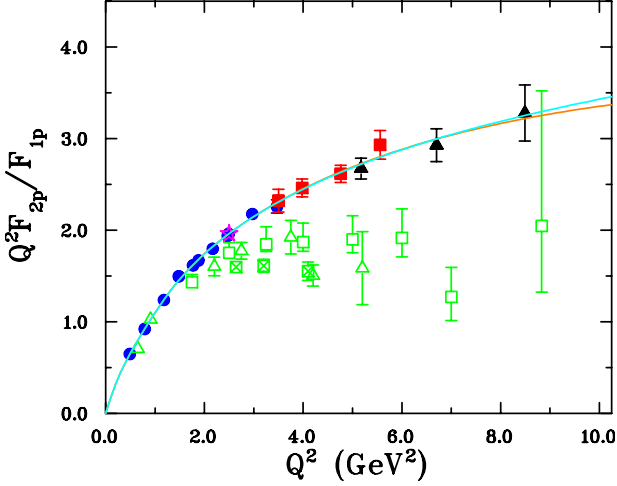


Fig. 12. Behavior of the ratio $Q^2 F_2/F_1$ for the proton, versus Q^2 . JLab data for recoil polarization; empty symbols for Rosenbluth data.

form factor is proportional to α_s/Q^4 times slowly varying logarithmic terms, because the momentum of the virtual photon absorbed by one quark, must be shared with the two other quarks through the exchange of two gluons. In lowest order the absorbed virtual photon cannot induce a quark helicity flip and consequently pQCD predicts a faster decrease of F_{2p} than of F_{1p} with increasing Q^2 , by a factor Q^{-2} [88]. The expectation is then that $Q^2 F_{2p}/F_{1p}$ should become constant at very high Q^2 . In Fig. ?? the JLab data together with data of Andivahis *et al.* [90,91], are shown as $Q^2 F_{2p}/F_{1p}$. The data from Ref. [90,91] show flattening above Q^2 of 3 GeV^2 . However, the data from this experiment do not show yet the specific pQCD Q^2 dependence.

Recently there have been two revisions of the pQCD prediction for the large Q^2 behavior of F_2 . In the first,

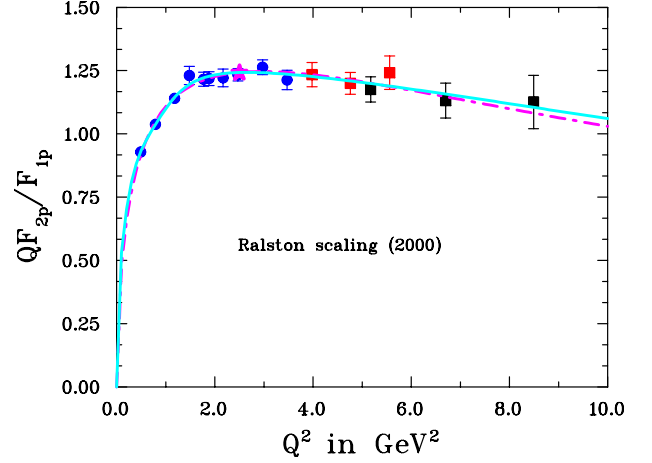


Fig. 13. Behavior of the ratio $QF_2.F_1$ for the proton, as discussed by Ralston, [86].

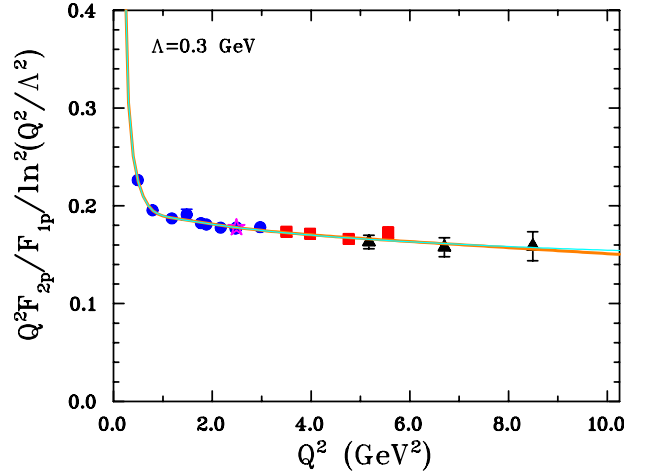


Fig. 14. Behavior of $Q^2 F_2/F_1/\ln^2(Q^2/\Lambda^2)$ as discussed by Belitsky [87].

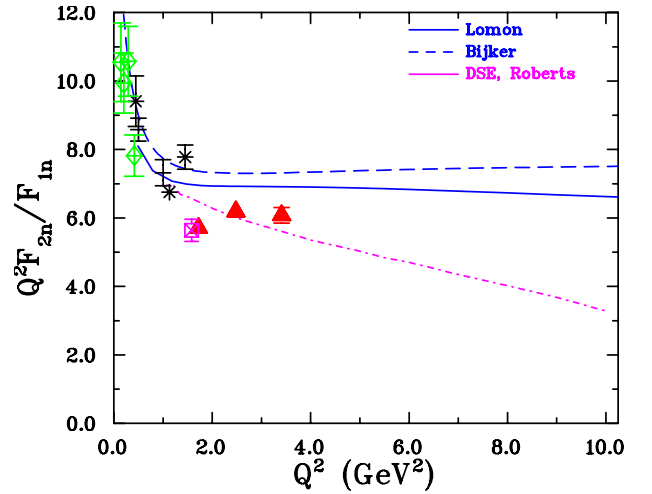


Fig. 15. Illustration of the current status on the asymptotic behavior of $Q^2 F_2/F_1$ for the neutron; all data ;points from double polarization experiments. “My Fit” needs to be verified.

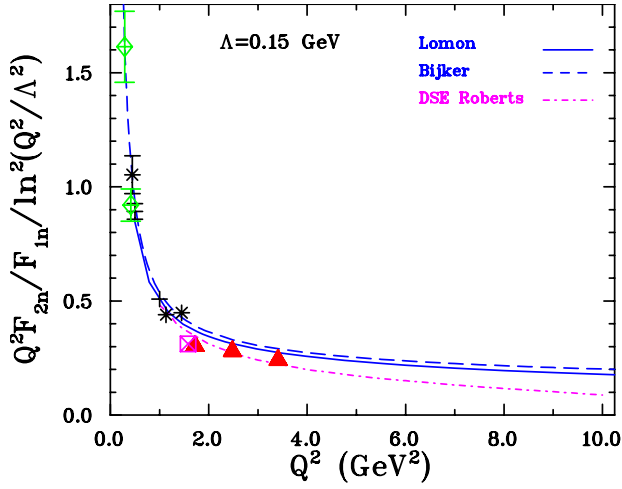


Fig. 16. The Belitzky plot for the neutron

Brodsky [92] argues that the pQCD motivated behavior of F_2 must contain an extra logarithmic term from higher twist contributions; the 3 free parameters a , b and c of the expression

$$\frac{F_{2p}}{F_{1p}} = \frac{1}{1 + (Q^2/c) \ln^b(1 + Q^2/a)} \quad (34)$$

were fitted in Ref. [92] to the data presented here augmented from the data of Ref. [30] with the result shown as a solid line in Fig. ?? . In the second, Belitsky *et al.* [87] reiterate the fact that the spin of a massless (or very light) quark cannot be flipped by the virtual photon of the ep reaction. For a quark to undergo spin-flip, it must be in a state of non-zero angular momentum with projection $|L_z|=1$. As a result, the standard pQCD prediction for F_{2p} (namely $\propto Q^{-6}$) becomes modified by a logarithmic term such that:

$$\frac{F_{2p}}{F_{1p}} = \frac{A}{\kappa_p Q^2} \ln^2\left(\frac{Q^2}{\Lambda^2}\right), \quad (35)$$

where A is a normalization constant; Λ is a cutoff constant required to suppress the infrared singularity generated by the very soft part of the quark wave function. Although the constant A in the expression above is not determined, a fit to the data of this paper augmented by the data of [30] gives $\Lambda = 290$ MeV, and $A = 0.175$. The soft physics scale of the nucleon is determined by Λ ; its size is of order of the transverse quark momentum in the nucleon. This fit is shown as the dashed line in Fig. ?? .

In Fig. ?? the JLab data plotted as QF_{2p}/F_{1p} show a remarkable flattening of the ratio starting at 1-2 GeV². Inspired by the results of this experiment, Ralston [93,86] revisited the calculation of the single-quark spin-flip amplitude responsible for the Pauli form factor in the framework of QCD and concluded that if quarks in the proton carry orbital angular momentum, then F_{2p}/F_{1p} should behave like $\frac{1}{\sqrt{Q^2}}$, rather than the well known pQCD prediction of $\frac{1}{Q^2}$ (Ref. [88]). In a different approach, Miller and

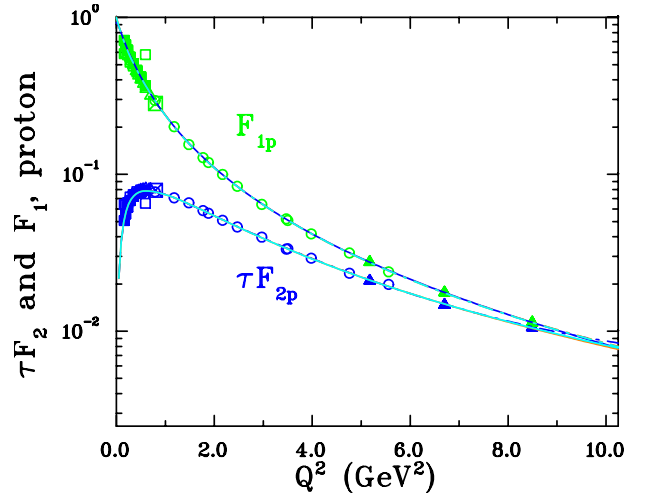


Fig. 17. The values of F_1 and τF_2 for the proton, obtained from the 3 JLab GEp experiments, and polynomial fits to them. From the definition of G_E , that form factor should cross zero when F_1 and τF_2 are equal. It can be seen that this condition is satisfied near $Q^2 = 10$ GeV². See also Fig 18.

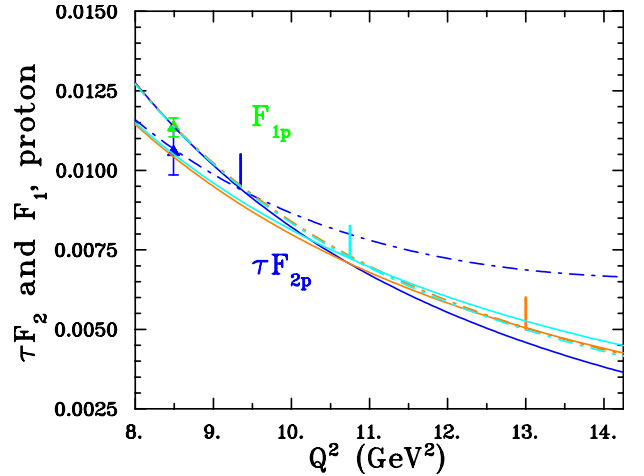


Fig. 18. Magnification of the $Q^2 = 12$ GeV² region of Fig. 22, showing 3 different positions for the zero crossing of G_E , marked as coloured vertical bars, for the 3 different fitting functions used: blue for an ad hoc polynomial of order 6 in Q , even and odd powers included; red ratio of polynomials with equal maximum power of Q^2 , hence asymptotically constant; green, same as last but with $\frac{1}{Q^2}$ asymptotic behavior.

Frank [94] have shown that imposing Poincaré invariance leads to violation of the helicity conservation rule, which results in the behavior of F_{2p}/F_{1p} observed in the JLab data.

6 Experimental Status

The two Sachs form factors, G_{Ep} and G_{Mp} , required to describe the nucleon charge- and magnetization distribution have been traditionally obtained by Rosenbluth separation

[?]. The G_{Mp} -data obtained by this method have shown good internal consistency up to 30 GeV². However, the characterization of G_{Ep} has suffered from large inconsistencies in the data base, which are now understood to be the result of the fast decrease of the contribution of G_{Ep} to the cross section. Although the structure of the proton has been taken for well known until recently, the experimental results from three GEp experiments from JLab showed that it held secrets which are only now being revealed.

The structure of the nucleons has been investigated experimentally with rigour over last 60 years using elastic electron scattering. The recent generation of electron accelerators with high polarization and high current electron beams, at MIT-Bates, the Mainz Microtron (MAMI), and the Continuous Electron Beam Accelerator Facility (CEBAF) of the Jefferson Lab (JLab), have made it possible to investigate the internal structure of the nucleon with extreme precision. In particular, the new generation of experiments that measures polarization variables like target asymmetry and recoil-polarization have allowed one to obtain the proton and neutron electromagnetic form factors accurately to large four momentum transfer, Q^2 . In this section we describe the form factors obtained from cross sections and double polarization experiments for proton and neutron.

6.1 Electron Scattering Cross Section Experiments

A recent experiment at the Mainz Microtron measured precision elastic cross-sections over a range of $Q^2 = 0.003$ to 1.0 GeV².

6.1.1 G_p^M - Dipole Form Factor Parametrization

6.1.2 G_p^E - Elastic Scattering Results

6.1.3 SuperRosenbluth Separation Results

Taking advantage of the high duty factor of modern accelerators, cross-sections can be measured to high precision over a range of ϵ in a relative short time period. Instead of detecting the elastically scattered electron, (e, e') , an experiment which detected the elastically scattered proton to identify elastic reactions, (e, p) , was run at Jefferson Lab in 2002. The same experimental approach of extraction the form factors by measuring elastic cross-sections at fixed Q^2 and different ϵ by varying the beam energy is used. The experimental method takes advantage of the fact that the proton momentum is constant for all epsilon at a fixed Q^2 . In addition for (e, p) , the detected proton rate and the radiation corrections have a smaller dependence on ϵ compared to (e, e') experiments. All this combines to reduce the ϵ dependent systematic error compared to (e, e') . The form factors were measured at $Q^2 = 2.64, 3.10$ and 4.60 GeV². In the Figure, the measurements of $\mu G_p^E/G_p^M$ from the (e, p) reactions are plotted compared to a global analysis of previous measurements from (e, e') experiments and the agreement between the

different methods is excellent. The plotted errors for the (e, p) data set are the combined statistical and systematic error and the error on the extraction of $\mu G_p^E/G_p^M$ has been improved by factors of two to three. The detection of scattered electrons or the scattered protons experiment techniques has different systematics, so the agreement between the two techniques indicate that experimental systematic error are understood.

With the success of the first Jefferson Lab (e, p) experiment, a subsequent experiment was run at Jefferson Lab in Hall C. The experiment measured cross-sections at a total of 102 kinematic settings covering a wide Q^2 range from 0.4 to 5.76 GeV² with at least three ϵ points per Q^2 . The emphasis was at each Q^2 to measure as wide an ϵ range as possible. At $Q^2 = 1$ GeV², thirteen ϵ points were measured ranging from $\epsilon = 0.05$ to 0.98, with eight of the points above $\epsilon = 0.8$. Similarly for At $Q^2 = 2.3$ GeV², ten ϵ points were measured ranging from $\epsilon = 0.07$ to 0.92, with five of the points above $\epsilon = 0.7$. The wide range of ϵ at a fixed Q^2 allows a check of the non-linearity in the ϵ dependence of the cross-section which would be a sign of two-photon exchange reactions effecting the cross-sections. The effects from two-photon exchange could have a dramatic ϵ dependence near $\epsilon = 1$.

6.1.4 G_n^M/G_n^E - QuasiElastic Scattering Results

6.2 Double Polarization Experiments

Indeed both the recoil polarization method, and asymmetry measurement using polarized target, has been used to measure the proton and the neutron form factors. Here we first describe the proton form factor results, and next the neutron form factor results.

6.2.1 Proton form factor results

The earliest polarization experiments, measuring polarization of recoil proton [13], and measuring asymmetry using polarized proton target [?], with unpolarized electron beams, were done to search for the two photon effects.

The first experiment with polarized electron beam and polarized target was done at the Stanford Linear Accelerator Center (SLAC) in 1970's [95]. This experiment measured the beam-target asymmetry $A = \frac{\sigma_{+-} - \sigma_{-+}}{\sigma_{++} + \sigma_{--}}$ at $Q^2 = 0.765$ GeV². The experiment concluded that the theoretical and experimental values are in good agreement if signs of G_{Ep} and G_{Mp} are the same.

The first experiment that used the recoil polarization method to measure the proton form factor ratio G_{Ep}/G_{Mp} was performed at the MIT-Bates laboratory [22,21]. In this experiment the proton form factor ratio G_{Ep}/G_{Mp} was measured for a free proton, and for a bound proton in a deuterium target at two $Q^2 = 0.38$ and 0.5 GeV². The success of this experiment elucidated that the recoil polarization transfer technique showed great promise for future measurements of G_E and G_M at higher Q^2 values for the proton and the neutron.

Next, using the same method of measuring recoil polarization in $^1\text{H}(e, e'p)$ reaction the ratio G_{Ep}/G_{Mp} was measured at the MAMI [19,96] at a Q^2 of $\approx 0.4 \text{ GeV}^2$. The ratio results were in agreement with other polarization measurements as well as Rosenbluth measurements.

In two experiments in Hall A at JLab the proton form factor ratios, G_{Ep}/G_{Mp} , were measured for Q^2 from 0.5 to 3.5 GeV^2 in 1998 and from 4.0 to 5.6 GeV^2 in 2000, using the recoil polarization method [27,30,28]. The ratios were also measured in 1990's in Hall A [50,97,98] at lower Q^2 values, as calibration measurements for other polarization experiments, and one measurement in Hall C [99], using the same method.

The first JLab experiment, GEp(1), measured the ratio, G_{Ep}/G_{Mp} , up to Q^2 of 3.5 GeV^2 [27,28]. In this experiment protons and electrons were detected in coincidence in the two high-resolution spectrometers (HRS) of Hall A [100]. The polarization of the recoiling proton was extracted from the azimuthal asymmetry measurement of the re-scattered proton in a graphite analyzer.

In the second JLab experiment, GEp(2), the ratio, G_{Ep}/G_{Mp} , was measured at $Q^2 = 4.0, 4.8$ and 5.6 GeV^2 with an overlap point at $Q^2 = 3.5 \text{ GeV}^2$ [30,101]. Several changes were made compared to the first experiment to extend the measurement to higher Q^2 . First, to increase the coefficient-of-merit (COM) of the focal plane polarimeter (FPP), a CH_2 analyzer was used instead of graphite; hydrogen has much higher analyzing power [102,103] than carbon [104], and to increase the fraction of events with a second scattering in the analyzer the thickness of the analyzer was increased from 50 cm of graphite to 100 cm of CH_2 . Second, to achieve complete solid angle matching with the HRS detecting the proton, a large frontal area lead-glass calorimeter was used to detect the electrons. The solid angle of the calorimeter was 6 times that of the HRS, at the largest Q^2 of 5.6 GeV^2 .

The proton form factor ratio also has been measured in a $^1\text{H}(e, e'p)$ reaction at a Q^2 of 1.51 GeV^2 by measuring the beam-target asymmetry in an experiment in Hall C at JLab in elastic ep scattering [105]. This is the highest Q^2 at which the G_{Ep}/G_{Mp} ratio has been obtained from a beam-target asymmetry measurement. This method was also used by the BLAST group at MIT-Bates [106]; this experiment measured the ratio at Q^2 values of 0.2 to 0.6 GeV^2 with high precision [106].

The results from the two JLab experiments [27,28,30], are plotted in Fig. 19 as the ratio $\mu_p G_{Ep}/G_{Mp}$ versus Q^2 , where they are also compared with Rosenbluth separation data [90,58,25,61,107–110,26]. As can be seen from figure 19, for the polarization data the statistical uncertainty is small; this is unlike the cross section data, where we see a large statistical uncertainty at higher Q^2 values, underlining the difficulties in obtaining G_{Ep} by the Rosenbluth separation method, as well as a large scatter in results from different experiments. The ratio G_{Ep}/G_{Mp} from polarization experiments decreases almost linearly with Q^2 , revealing a definite difference between the spatial distributions of charge and magnetization at short distances. These results were very surprising at the time (1998-2002),

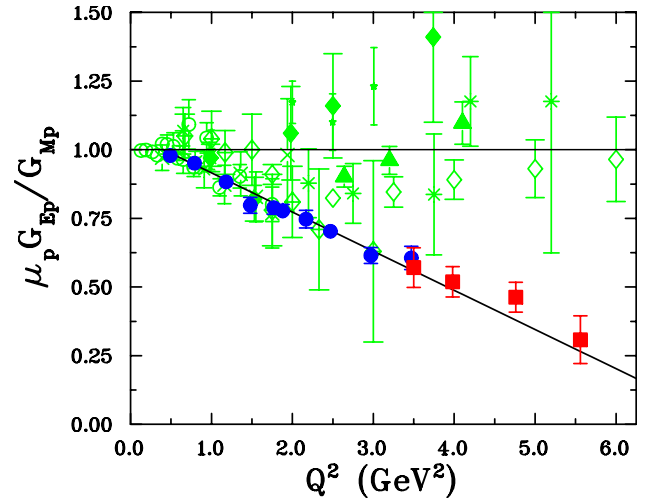


Fig. 19. The ratio $\mu_p G_{Ep}/G_{Mp}$ from the two JLab experiments [30,28] (filled circle and square), and other polarization experiments, compared to Rosenbluth separation results; JLab Rosenbluth results from [58,25] shown as open and filled triangles, respectively. The cross section data in Figs. 7 and ?? (open circles).

as they appeared to contradict the consensus based on Rosenbluth separation results up to 6 GeV^2 by Andivahis *et al.* [90] that demonstrated that the ratio, $\mu_p G_{Ep}/G_{Mp}$, remains close to 1 as illustrated in Fig. 19.

The results from the two JLab experiments [27,28,30] showed conclusively for the first time a clear deviation of the proton FF ratio from unity, starting at $Q^2 \simeq 1 \text{ GeV}^2$; older data from [107,109,108,110] showed such a decreasing ratio, but with much larger statistical and systematic uncertainties, as seen in Fig. 19. The most important feature of the JLab data, is the sharp decrease of the ratio $\mu_p G_{Ep}/G_{Mp}$ from 1 starting at $Q^2 \approx 1 \text{ GeV}^2$ to a value of ~ 0.28 at $Q^2 = 5.6 \text{ GeV}^2$, which indicates that G_{Ep} falls faster with increasing Q^2 than G_{Mp} . This was the first definite experimental indication that the Q^2 dependence of G_{Ep} and G_{Mp} is different.

The two methods, Rosenbluth and polarization, give definitively different results; the difference cannot be bridged by either simple re-normalization of the Rosenbluth data [111], or by variation of the polarization data within the quoted statistical and systematic uncertainties. This discrepancy has been known for sometime now, and has been the subject of discussion and investigation. A possible explanation is the hard two-photon exchange process, which affects both cross section and polarization transfer components at the level of only a few percents; however, the contribution of the two-photon process has drastic effect on the Rosenbluth separation results, whereas it modifies the ratio obtained with the polarization method by a few percent only. This will be discussed in detail in ??.

Following the unexpected results from the GEp(1) and GEp(2) polarization experiments at JLab, a new experiment, GEp(3) was approved to extend the Q^2 -range to 9 GeV^2 in Hall C at JLab. Two new detectors were built

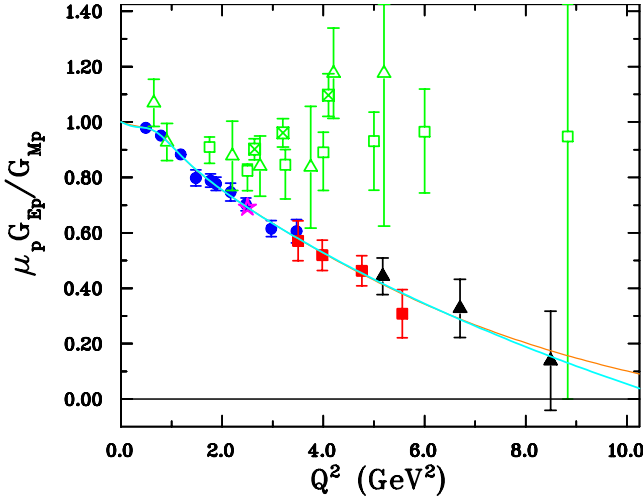


Fig. 20. All data for the ratio G_{Ep}/G_{Mp} obtained from the three large Q^2 recoil polarization experiments at JLab and all other double polarization experiments. The dot-dashed curve is a 4 parameter fit without constrain at $Q^2=0$, the solid line is a 7 parameter fit with ratio constrained to 1 at $Q^2=0$; Both fits are of the Kelly type, polynomial over polynomial, with $1/Q^2$ behavior at large Q^2 .

to carry out this experiment; a large solid-angle electromagnetic calorimeter and a double FPP. The recoil protons were detected in the high momentum spectrometer (HMS) equipped with the new double FPP. The scattered electrons were detected in a new lead glass calorimeter (BigCal) built for this purpose out of 1744 glass bars, 4x4 cm² each, giving a total frontal area of 2.6 m², which provided complete kinematical matching to HMS solid angle. This experiment was completed in the spring of 2008 and measured the form factor ratio at Q^2 of 5.2, 6.7 and 8.5 GeV². The data analysis was completed in 2010 and the results were published [112].

Figure 20 shows the results from three JLab experiments [27,30,28,112], as well as results of all other double polarization experiments [22, 50, 19, 96–99, 105, 106, 113], as the ratio $\mu_p G_{Ep}/G_{Mp}$ versus Q^2 . All data show only the statistical uncertainty. As can be seen from figure 20, data from different experiments are in excellent agreement, this is unlike G_{Ep} obtained from cross section data.

The striking feature of the results of the GEp(3) experiment is a continued, strong and almost linear decrease of the ratio with increasing Q^2 , albeit with some indication of a slowdown at the highest Q^2 . The overlap point at 5.2 GeV² is in reasonably good agreement with the two surrounding points from Gayou *et al.* [50]. The GEp(3) experiment used a completely different apparatus in a Q^2 range where direct comparison with the Hall A recoil polarization results is possible. The comparison provides an important confirmation of the reproducibility of the results with the recoil polarization technique using a completely different apparatus. Additionally, the results of the high-statistics survey of the ϵ -dependence of G_{Ep}/G_{Mp} at $Q^2 = 2.5$ GeV², from the GEp(2 γ) experiment [114]

shown as magenta star in Fig. 20 is in excellent agreement with the results from GEp(1) experiment in Hall A [28] at $Q^2 = 2.47$ GeV².

Fig. ?? shows the ratio of the Pauli and Dirac form factors, F_2 and F_1 , multiplied by Q^2 , which can be obtained directly from the ratio G_{Ep}/G_{Mp} , without requiring any additional information; this is the second interesting result of this experiment: the ratio $Q^2 F_2/F_1$ does not show an obvious tendency to become constant, as the original perturbative QCD prediction of Brodsky et al [88] implied.

6.3 Discrepancies between Cross Section and Polarization Results

6.3.1 Results from the G_p^E -2 γ Experiment

6.3.2 Preliminary Results from the Hall B e^+/e^- Experiment

6.3.3 Preliminary Results from the OLYMPUS Experiment

6.3.4 Theoretical Interpretation of Two-Photon Exchange Results

6.4 Proton Charge Radius Experiments

6.4.1 Past Results

6.4.2 Future Experiments

6.5 Flavor Separation Experiments

7 Theoretical Interpretations of Nucleon Form Factors

Placeholder text.

In this section we give an overview of the theoretical understanding of the nucleon e.m. FFs. These FFs encode the information on the structure of a strongly interacting many-body system of quarks and gluons, such as the nucleon. This field has a long history and many theoretical attempts have been made to understand the nucleon FFs. This reflects the fact that a direct calculation of nucleon FFs from the underlying theory, Quantum Chromodynamics (QCD), is complicated as it requires, in the few GeV momentum transfer region, non-perturbative methods. Hence, in practice it involves approximations which often have a limited range of applicability. Despite their approximations and limitations, some of these non-perturbative methods do reveal some insight in the nucleon structure.

The earliest models to explain the global features of the nucleon FFs, such as its approximate dipole behavior, were vector meson dominance (VMD) models which are discussed in Sect. ?? In this picture the photon couples to the nucleon through the exchange of vector mesons. Such VMD models are a special case of more general dispersion relation fits, which allow to relate time-like and space-like

FFs, and which are discussed subsequently.

To understand the structure of the nucleon in terms of quark and gluon degrees of freedom, constituent quark models have a long history. We discuss the intricacies in describing a bound system of relativistic constituent quarks and review the resulting predictions for FFs in Sect. ???. Despite some of their successes, models based on quarks alone do suffer from the evident shortcoming that they do not satisfy the global chiral symmetry of QCD when rotating left and right handed light quarks in flavor space. This chiral symmetry is broken spontaneously in nature, and the resulting Goldstone bosons are pions. Since they are the lightest hadrons, they dominate the low momentum transfer behavior of form factors, and manifest themselves in a pion cloud surrounding the nucleon. Such pion cloud models will also be discussed in Sect. ??.

In Sect. ??, we discuss the spatial information which can be obtained from the nucleon FFs, and discuss both radial densities and the issue of shape of the nucleon.

Sect. ?? describes the chiral effective field theory of QCD and their predictions for nucleon FFs at low momentum transfers, where such perturbative expansions are applicable.

In Sect. ??, we shall discuss the lattice QCD simulations, which have the potential to calculate nucleon FFs from first principles. This is a rapidly developing field and important progress has been made in the recent past. Nevertheless, the lattice calculations are at present still severely limited by available computing power and in practice are performed for quark masses sizably larger than their values in nature. We will discuss the issues in such calculations and compare recent results. It will also be discussed how the chiral effective field theory can be useful in extrapolating present lattice QCD calculations to the physical pion mass.

In Sect. ??, we discuss the quark structure of the nucleon and discuss generalized parton distributions (GPDs) of the nucleon. These GPDs are being accessed in hard exclusive reactions, which allow to remove in a controlled way a quark from the initial nucleon and implanting instead another quark in the final nucleon. The resulting GPDs can be interpreted as quark correlation functions and have the property that their first moments exactly coincide with the nucleon FFs. We discuss the information which has been obtained on GPDs from fits of their first moments to the precise FF data set.

Finally, in Sect. ??, we discuss the nucleon FFs in the framework of perturbative QCD. These considerations are only valid at very small distances, where quarks nearly do not interact. In this limit, the nucleon FFs correspond to a hard photon which hits a valence quark in the nucleon, which then shares the momentum with the other (near collinear) valence quarks through gluon exchange. We discuss the predictions made in this limit and confront them with the experimental status for Dirac and Pauli FFs at large momentum transfers.

7.1 Models of Nucleon Form Factors

7.1.1 Conformal fits to Form Factors

There has been a lively, at least to those engaged in it, discussion of what sorts of functions to use in fitting the form factors. Simple polynomial fits, for example, will not converge for moderate or large momentum transfers. The reason flows from the fact that the form factors are, from a mathematical viewpoint, analytic functions of their argument $Q^2 = -q^2$, except for cuts at known locations. The cuts are on the timelike side, and begin where one can have a photon to two pion transition at $q^2 = 4m_\pi^2$. A cut can be viewed as a weighted continuum of poles, so that there is a contribution to the form factor containing a factor $1/(q^2 - 4m_\pi^2)$. The weighting of this pole may be weak, but in principle its existence means that a polynomial expansion of the form factor will not converge for $Q^2 \geq 4m_\pi^2$. It is like the expansion of the geometric series $1/(1-x)$, which does not converge for $|x| \geq 1$; simply replace x by $q^2/(4m_\pi^2)$.

However, it is possible to make a mapping of Q^2 to another variable, denote it z , where a polynomial expansion in z is allowed. The trick is to find a transformation where spacelike momentum transfers all map onto the real line $|z| < 1$ and timelike momentum transfers map onto the circle $z = 1$ (in the complex z -plane). Then since all poles of the form factors lie on the unit circle in z , a polynomial expansion in z is convergent everywhere inside the unit circle, *i.e.*, for all spacelike momentum transfers.

This trick has been applied in the context of Weak interaction form factors, as for semileptonic meson decay, for some time [115, 116]. It has more recently been applied to fitting electromagnetic form factors [117, 118].

The variable z can be given by the conformal mapping [117, 118], with $t = q^2$,

$$z(t, t_{\text{cut}}) = \frac{\sqrt{t_{\text{cut}} - t} - \sqrt{t_{\text{cut}}}}{\sqrt{t_{\text{cut}} - t} + \sqrt{t_{\text{cut}}}}, \quad (36)$$

where $t_{\text{cut}} = 4m_\pi^2$ and one can easily enough verify that the mapping has the properties stated above.

Fitting with a nonconvergent expansion can give good analytic fits to the data in any region where there is data to be fit. The danger lies in extending them outside the region where there is data. Such extrapolations can go awry, sometimes diverging wildly from physical expectation and sometimes, depending on how far one extrapolates, there may be problems that are less visible. Here enters also the proton radius question, whose evaluation from form factors requires an extrapolation from the lowest Q^2 where there is data down to $Q^2 = 0$. Extrapolating a fit made with an intrinsically convergent expansion is arguable safer.

The two fits made to the electromagnetic form factors using the conformal variable z , however, differ in their conclusions regarding the proton charge radius. The earlier fit [117] used electron-proton scattering data available before the Mainz experiment [119] published in 2010. They found a proton radius $R_E^p = 0.870 \pm 0.023 \pm 0.012$, so

their central value is closer to the CODATA value than to the muonic Lamb shift value. The other fit [118] used the 1422 data points from the Mainz experiment, and obtained $R_E^p = 0.840 \pm 0.015$ fm (see also [120]).

7.1.2 Vector Meson Dominance (VMD)

Placeholder text

The starting point in understanding the interaction of a vector probe such as the photon with a hadronic system is provided by the observation that the lowest lying hadrons with vector quantum numbers are the vector mesons $\rho(770)$, $\omega(782)$ and $\phi(1020)$. In the process $e^+e^- \rightarrow \text{hadrons}$, these vector mesons show up as prominent resonances at the corresponding values of the e^+e^- squared *c.m.* energy $q^2 > 0$. One therefore expects that in the elastic electron scattering process on the nucleon, $eN \rightarrow eN$, the nucleon electromagnetic FFs at low space-like momentum transfers, $q^2 < 0$, will be dominated by these lowest lying singularities from the time-like region. A large class of models for F_1 and F_2 are based on this vector meson dominance (VMD) hypothesis, as depicted in 21.

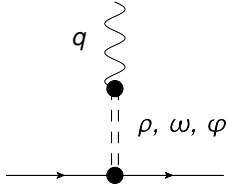


Fig. 21. The vector meson dominance picture for the coupling of the photon (with four-momentum q) to a nucleon.

Within such VMD models, the approximate dipole behavior of the nucleon e.m. FFs, see Eq. (3), can be understood as being due to the contribution of two nearby vector meson poles which have opposite residues. Assume that one considers two vector meson pole contributions in 21 (with masses m_{V1} and m_{V2} and residues of equal magnitude and opposite sign a and $-a$ respectively), one obtains :

$$\begin{aligned} F_{1,2}(q^2) &\sim \frac{a}{q^2 - m_{V1}^2} + \frac{(-a)}{q^2 - m_{V2}^2} \\ &= \frac{a(m_{V1}^2 - m_{V2}^2)}{(q^2 - m_{V1}^2)(q^2 - m_{V2}^2)}. \end{aligned} \quad (37)$$

An early VMD fit was performed by Iachello *et al.* [?] and predicted a linear decrease of the proton G_{Ep}/G_{Mp} ratio, which is in basic agreement with the result from the polarization transfer experiments. Such VMD models have been extended by Gari and Krümpelmann [?] to include the perturbative QCD (pQCD) scaling relations [89], which state that (see Sect. ??) $F_1 \sim 1/Q^4$, and $F_2/F_1 \sim 1/Q^2$.

In more recent years, extended VMD fits which provide

a relatively good parameterization of all nucleon e.m. FFs have been obtained. An example is Lomon's fit [59], using $\rho(770)$, $\omega(782)$, $\phi(1020)$, and $\rho'(1450)$ mesons and containing 11 parameters. Another such recent parameterization by Bijker and Iachello [60] including $\rho(770)$, $\omega(782)$, and $\phi(1020)$ mesons only achieves a good fit by adding a phenomenological contribution attributed to a quarklike intrinsic *qqq* structure (of *rms* radius ~ 0.34 fm) besides the vector-meson exchange terms. The pQCD scaling relations are built into this fit which has 6 free parameters which are fit to the data. In contrast to the early fit of Ref. [?], the new fit of Ref. [60] gives a very good description of the neutron data, albeit at the expense of a slightly worse fit for the proton data.

It will be interesting to check the resulting VMD fits for the neutron FFs to larger Q^2 . In this regard, an interesting “prediction” can be drawn when the FFs F_2 and F_1 obtained directly from double polarization experiments are shown in the same graph for the proton and the neutron, as in Fig. 22. It is remarkable that both F_1 and F_2 tend toward the same value for proton and neutron, and may meet at a Q^2 value which will soon be accessible for the neutron. This conclusion is influenced by the VMD fits shown in the same figure, and rests on their extrapolation for the neutron to larger Q^2 . Note that the VMD fits shown include all data for p and n, but selects the recoil polarization over the Rosenbluth results for Q^2 larger than 1 GeV^2 .

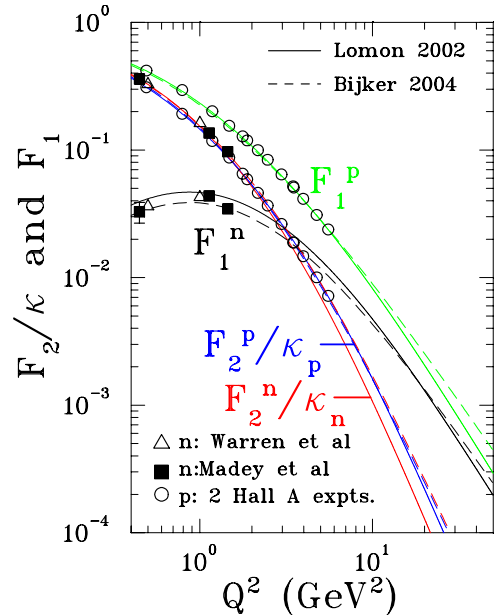


Fig. 22. The FFs F_1 and F_2 for the proton and the neutron obtained from double polarization experiments only. The values of F_2 and F_1 were obtained from the experimental FF ratios using fitted values to the data base for G_{Mp} and G_{Mn} . For the proton data, the fit from [121] was used; for the neutron data in [84] the fit from [121], and in [73] the fit from [122] were used. The curves are the VMD fits of Lomon [59] and of Bijker and Iachello [60].

7.1.3 Dispersion Analyses

Newer works here include the dispersive analyses of the nucleon form factors by workers in Bonn [123,118,120]. Older works include [124–126]. The works include general analyses and fits to the form factors, as well as aspects directly aimed at the resolution of the proton radius puzzle [123,118,120].

Dispersion relations relate the form factors in the space-like and timelike regions. More generally, the form factors are complex functions of q^2 that are analytic except for known cuts, and the form factors anywhere can be calculated if one knows just their imaginary parts at the cuts. The cuts are all on the real axis for timelike q^2 . The cuts run from $q^2 \approx 4m_\pi^2$ to $q^2 = \infty$. In practice, one cannot know the imaginary part of the form factors over this whole range, and uncertainty in knowing the form factors in the timelike region builds nonlinearly to larger uncertainty in predicting the form factors in the spacelike region, especially at higher Q^2 .

At lower Q^2 , one specific boon of the dispersive treatment is that the connection between the timelike and spacelike regions puts an extra constraint on the form factors and their slope at spacelike threshold. This means that the determination of the charge and magnetic radii are not purely extrapolations of the scattering data, but is an interpolation in this procedure and hence arguably more reliable.

A technique for using the dispersion relations, used by both [124] and by [123], is to parameterize the imaginary part of the timelike form factors, and determine the parameters by making a least squares fit to the known spacelike and timelike data. One thereby obtains a representation of the form factors that one can use in regions where there is not yet data.

Ref. [124], published in 2006, applies dispersion relations to the ratio G_E^p/G_M^p , with the assumption of no zeros in G_M^p . They used some large-uncertainty-limit G_E^p/G_M^p data in the timelike region, obtained from angular distributions in $e^+e^- \rightarrow p\bar{p}$ or the reverse, to supplement the polarization data in the spacelike region. One of the main goals was to compare to models that fit the spacelike data, especially to the continuations of those models to the timelike regions [127].

They found that there was a zero in $G_E^p(q^2)$ at about 11 GeV² spacelike momentum transfer squared, and found that the Phragmén-Lindelöf theorem, which leads to the statement that $|G_E^p(q^2)/G_M^p(q^2)|$ should be the same at very large momentum transfers, whether spacelike or timelike, was satisfied, albeit with opposite signs. Many of the more purely phenomenological models differed on the latter point. This work [124] preceded the completion of the polarization experiments at the highest current Q^2 [112, 101]. The dispersive aspects have not been updated in more recent works by some of the same authors, *e.g.* [126], but one can see that the results would not be materially changed by the newer data.

Ref [123], which is an updated version of [125], applies the dispersion analysis to G_E^p and G_M^p separately. An important improvement in the newer work [123] is that it

includes the recent Mainz data [119] in its fit. A salient outcome of this analysis is that the proton charge radius comes out at a value $R_E^p = 0.84(1)$ fm, in agreement with the value found in the muon hydrogen Lamb shift measurement.

7.1.4 Constituent Quark Models

Placeholder text

In our quest to understand the structure of the nucleon in terms of the quark and gluon degrees of freedom which appear in the QCD Lagrangian, constituent quark models (CQMs) have a long history, which predates the establishment of the theory of strong interactions, QCD. In a CQM, the nucleon appears as the ground state of a quantum-mechanical three-quark system in a confining potential. In such a picture, the ground state baryons (composed of the light up (u), down (d) and strange (s) quark flavors) are described by $SU(6)$ spin-flavor wave functions (WFs), supplemented by an antisymmetric color WF.

In the Isgur-Karl model [?], the constituent quarks move in a harmonic oscillator type confining potential. For the ground state baryons, the three constituent quarks are in the 1s oscillator ground state, corresponding to the [56]-plet of $SU(6)$. In the Isgur-Karl model, the long-range confining potential is supplemented by an interquark force corresponding to one-gluon exchange. The one-gluon exchange leads to a color hyperfine interaction between quarks, which breaks the $SU(6)$ symmetry and leads to a mass splitting between $N(939)$ and $\Delta(1232)$, often referred to as the hyperfine splitting. It was found that it also predicts well the mass splittings between octet and decuplet baryons [128]. Furthermore, the color hyperfine interaction leads to a tensor force which produces a small D -state ($L = 2$) admixture in the N (as well as Δ) ground states [?,129], corresponding to a D -state probability in the N ground state around 0.2 %. Even though such D -wave probability is small, it leads to a non-spherical charge distribution. For a static charge distribution, a measure of the non-sphericity (or deformation) is given by its quadrupole moment. Since the nucleon has spin 1/2, an intrinsic quadrupole moment of the nucleon cannot be directly measured because angular momentum conservation forbids a non-zero matrix element of a ($L = 2$) quadrupole operator between spin 1/2 states. However this quadrupole deformation may reveal itself in an electromagnetically induced transition from the spin 1/2 N to the spin 3/2 Δ state. In this way, the tensor force between quarks gives rise to non-zero values for the electric quadrupole ($E2$) and Coulomb quadrupole ($C2$) transitions¹.

The non-relativistic CQM, despite its simplicity, is quite successful in predicting the spectrum of low-lying baryons, and gives a relatively good description of static properties such as the octet baryon magnetic moments. To calculate the FFs of a system of constituents with masses small

¹ The relation between the tensor force, D -wave admixture, and the electromagnetic $N \rightarrow \Delta$ transition was already pointed out in the early paper of Glashow [130]. An up-to-date discussion of this field can be found in the review of [131].

compared with the confinement mass scale necessitates however a relativistic treatment even for low momentum transfers. For momentum transfers several times the nucleon mass squared a relativistic description becomes crucial.

In contrast to the calculation of the spectrum, which uses eigenfunctions of a Poincaré invariant mass operator, a calculation of the nucleon electromagnetic FFs requires the relation between the rest frame spin and momenta (in the three-quark WF) and those in the moving frame. This requires an extension of eigenfunctions of the spin and mass operators, so as to transform consistently under the unitary representations of the Poincaré group. The way to implement relativity into a Hamiltonian formalism (describing e.g. a system of three interacting constituent quarks) has been laid out by Dirac [132]. There are three *forms of dynamics* (so called instant, point, and light-front forms) which differ in the choice of the kinematical subgroup of the Poincaré group. This is the subgroup of the Poincaré group whose commutator relations are not affected by the interactions between the constituents. The three (unitarily equivalent) forms therefore differ by which of the ten generators of the Poincaré group (four space-time translations, three spatial rotations, and three boosts) are kinematical (i.e. interaction free), and which are dynamical, i.e. depend on the interactions and necessarily have to be approximated in a practical calculation.

In the *instant form*, the dynamical generators are the time component of the four-momentum and the three boost operators. Rotations do not contain interactions, which makes it easy to construct states of definite angular momentum in this form.

In the *point form*, both boosts and rotations are kinematical. The point-form therefore has the important technical advantage that the angular momenta and Lorentz boosts are the same as in the free case. However all four components of the four-vector operator are dynamical in this form.

In the *light-front form*, seven of the generators of the Poincaré group are kinematical (this corresponds to the symmetry group of a null plane), which is the maximum number possible. The remaining three dynamical generators which contain the interactions are one component of the four-momentum operator (the so-called light-cone Hamiltonian) and 2 transverse rotations. Light-front (as well as point form) calculations for relativistic CQMs are convenient as they allow to boost quark WFs independently of the details of the interaction. The drawback of the light-front calculations however is that because two generators of rotations are dynamical, the construction of states with good total angular momentum becomes interaction dependent.

Any practical calculation in one of the three forms approximates the current operator. The common (so-called impulse) approximation is that the photon interacts with a single quark in the nucleon.

The light-front form calculation of nucleon FFs has been pioneered by Berestetsky and Terentev [?], and more recently developed by Chung and Coester [133]. In prac-

tice one starts from a rest frame nucleon WF for the three-quark state which ideally is fitted to the baryon spectrum. The nucleon WF in the light-front form (so-called light-front WF) is obtained by a Melosh rotation [134] of each of the quark spinors, connecting the instant and light-front forms. When performing the front form calculation in a (Drell-Yan) frame where the photon light-cone momentum² component $q^+ = 0$, the space-like virtual photon only connects Fock components in the nucleon light-front WFs with the same number of constituents, i.e. matrix elements between qqq and $qqqq\bar{q}$ states which would be present in an instant form calculation are zero in the light-front calculation. This property allows for a consistent calculation within the light-front formalism when truncating the Fock space to only the three-quark state.

In [133] a Gaussian WF in the quark internal (transverse) momentum variables was used. Although this model yields a surprisingly good agreement for the observed G_{Ep}/G_{Mp} ratio, see 23, it yields nucleon FFs which drop too fast at larger Q^2 values when using constituent quark masses around 330 MeV. Schlumpf [?] allowed for high momentum components in the nucleon light-front WF by adopting a power law dependence in the quadratic quark internal momentum variables. The two parameters in Schlumpf's WF were fitted to magnetic moments and semi-leptonic decays of the baryon octet. The resulting e.m. FF calculations reproduce reasonably well the power behavior of the FF at larger Q^2 . The WF of Schlumpf was also used by Frank, Jennings, and Miller [135,94]. They found that such a light-front WF leads to a violation of hadron helicity conservation resulting in a F_{2p}/F_{1p} ratio which drops less fast than $1/Q^2$ [94], in agreement with the G_{Ep}/G_{Mp} polarization data.

The WFs in the calculations described above were however not constructed from a detailed fit to the baryon spectrum. Cardarelli *et al.* subsequently performed a more "microscopic" light-front calculation [136,137] where the light-front WF was obtained from a rest frame WF which provided a fit to the spectrum. The rest frame WF was taken from the relativized Capstick-Isgur model [140]. Using this WF, the constituent quark momentum distribution in the nucleon was found to yield an important content of high-momentum components, which are generated by the short-range part of the quark-quark interaction, which is due to one-gluon exchange in the Capstick-Isgur model. These components are completely absent if one only considers the linear confinement potential in the model.

In a CQM calculation, the effect of other degrees of freedom beyond three quarks are buried within the constituent quarks, which are considered as quasi-particles. In the absence of a microscopic calculation, such effects are parameterized in terms of constituent quark FFs. In [?], it was shown that the data for the proton unpolarized forward structure function at low momentum transfers exhibits a new scaling property and can be interpreted as quasi-elastic scattering off extended constituent quarks inside the proton described by a constituent quark FF.

² Defining light-cone components as $x^\pm = (x^0 \pm x^3)/\sqrt{2}$ and defining the null-plane by $x^+ = 0$.

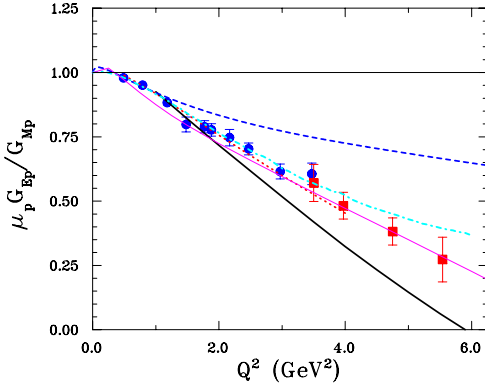


Fig. 23. Comparison of relativistic CQM calculations with the data for $\mu_p G_{Ep}/G_{Mp}$. Dotted curve : front form calculation of Chung and Coester [133] with point-like constituent quarks; thick solid curve : front form calculation of Frank *et al.* [135]; dot-dashed curve : front form calculation of Cardarelli *et al.* [136, 137] with point-like constituent quarks; dashed curve : point form calculation of Boffi *et al.* [138] in the Goldstone boson exchange model with point-like constituent quarks; thin solid curve : covariant spectator model of Gross and Agbakpe [139]. The data are from [?] (solid circles) and [?] (empty squares).

The resulting constituent size is around 0.2 - 0.3 fm. Using such effective constituent quark FF in the light-front form calculation of [137], allows a good description of the individual nucleon FFs, see [141]. Note however that the experimental G_{Ep}/G_{Mp} ratio can basically be reproduced using point-like constituent quarks, see 23. The suppression of the G_{Ep}/G_{Mp} ratio with respect to the dipole-fit as predicted in the light-front form CQM calculation is attributed to relativistic effects generated by the Melosh rotations of the constituent quark spins. These Melosh rotations introduce kinematical $SU(6)$ breaking effects in addition to the dynamical $SU(6)$ breaking due to the (hyperfine) one-gluon exchange potential.

A comparable amount of high-momentum components in the nucleon WF was obtained in the Goldstone-boson-exchange (GBE) quark model [142, 143]. This model relies on constituent quarks and Goldstone bosons, which arise as effective degrees of freedom of low-energy QCD from the spontaneous breaking of the chiral symmetry. The resulting CQM assumes a linear confinement potential supplemented by a quark-quark interaction based on the exchange of pseudoscalar Goldstone bosons, which is the source of the hyperfine interaction. It was shown in [142, 143] that the GBE CQM yields a unified description of light- and strange-baryon spectra. The GBE CQM was used in [144, 138] to calculate the nucleon e.m. FFs in the point-form. The neutron charge radius is well described in this model and is driven by the mixed-symmetry component in the neutron WF. In contrast to the light-front calculation [137, 141], it was found that when performing a point-form calculation of the nucleon e.m. FFs at larger Q^2 within the impulse approximation, i.e. considering only single-quark currents, a surprisingly good overall description of the nucleon e.m. FFs can be obtained, us-

ing point-like constituent quarks only. When looking at details of Refs. [144, 138], the agreement is worse though for G_{Mp} which is underpredicted at larger Q^2 , and the ratio of G_{Ep}/G_{Mp} is overpredicted at larger Q^2 , see 23. Similar findings have also been obtained in the point-form calculation of [145] for the OGE CQM. The overall success of the point-form result using point-like constituent quarks was attributed in [144, 138, 145] to the major role played by relativity. Such a finding is remarkable in view of the expected finite size of the constituent quarks, as discussed above.

An explanation for the above finding for the nucleon e.m. FFs in the point form, using the single-quark current approximation, has been suggested by Coester and Riska [146]. When the spatial extent of the three-quark WF is scaled (unitarily) to zero, both instant- and front-forms yield FFs independent of the momentum transfer. Therefore, to reproduce the experimental fall-off of the nucleon e.m. FFs at large momentum transfers requires the introduction of constituent quark FFs. In contrast, when the WF in point form is scaled unitarily to zero (so-called point limit), a non-trivial scaling limit is obtained for the FFs, depending on the shape of the WF. At high values of momentum transfer, the scaled FFs decrease with an inverse power of the momentum transfer. The power is determined by the current operator and is independent of the WF. An explicit comparative calculation of the baryon e.m. FFs between the three different forms was performed in [147] using a simple algebraic form for the three-quark WF, depending on two parameters. It was verified that a qualitative description of the nucleon FF data demands a spatially extended WF in the instant- and front-form descriptions, in contrast to the point-form description which demands a much more compact WF.

A manifestly covariant CQM calculation within the Bethe-Salpeter formalism and using an instanton-induced interaction between quarks has been performed by Merten *et al.* [148]. Although this model reproduces the baryon spectrum, it can only qualitatively account for the Q^2 dependence of the nucleon e.m. FFs.

Another covariant CQM calculation was performed by Gross and Agbakpe [139], using a covariant spectator model. Assuming a simple pure S -wave form for the nucleon three-quark wave function, evaluating the current matrix element in a relativistic impulse approximation, and assuming constituent quark FFs including a phenomenological term which parameterizes the pion cloud, an eleven parameter description of the nucleon FF data was obtained, see 23.

As a next step for CQMs, it would clearly be very worthwhile to investigate the approximations in the current operator within each form. The quality of the commonly made impulse approximation may differ between the different forms. Within the context of a toy model calculation in Refs. [149, 150], it has e.g. been shown that the neglect of two-body currents in the point form does affect the FFs in a more drastic way than their neglect in the instant or light-front forms.

The importance of two-body currents has also been

shown in the work of De Sanctis *et al.* [151]. In that work, a calculation within the hypercentral CQM was performed of the (two-body) quark pair contribution to the e.m. current resulting from the one-gluon exchange interaction between the quarks. This pair current contribution was found to lead to a sizeable reduction of G_{Ep} compared with G_{Mp} .

7.1.5 Pion Cloud Models

Placeholder text

Despite their relative success in describing the spectrum and structure of low-lying baryons, models based on constituent quarks alone suffer from evident shortcomings as they do not satisfy all symmetry properties of the QCD Lagrangian. In nature, the up and down (current) quarks are nearly massless. In the exact massless limit, the QCD Lagrangian is invariant under $SU(2)_L \times SU(2)_R$ rotations of left (L) and right (R) handed quarks in flavor space. This *chiral symmetry* is spontaneously broken in nature leading to the appearance of massless Goldstone modes. For two flavors, there are three Goldstone bosons — pions, which acquire a mass due to the explicit breaking of chiral symmetry by the current quark masses.

Since pions are the lightest hadrons, they dominate the long-distance behavior of hadron WFs and yield characteristic signatures in the low-momentum transfer behavior of hadronic FFs. Therefore, a natural way to qualitatively improve on the above-mentioned CQMs is to include the pionic degrees of freedom [152].

An early quark model with chiral symmetry is the chiral (or, cloudy) bag model. This model improves the early MIT bag model by introducing an elementary, perturbative pion which couples to quarks in the bag in such a way that chiral symmetry is restored [153]. Within the cloudy bag model, Lu *et al.* [154] performed a calculation of the nucleon e.m. FFs improving upon previous calculations by applying a correction for the center-of-mass motion of the bag. This calculation also implemented Lorentz covariance in an approximate way by using a prescription for the Lorentz contraction of the internal structure of the nucleon. Using a bag radius $R \simeq 1$ fm, this model provides a good description of the nucleon e.m. FFs in the range $Q^2 < 1$ GeV².

To extend such a calculation to larger Q^2 , Miller performed a light-front cloudy bag model calculation [155]. Starting from a model in terms of constituent quarks [94], described by the light-front WF of Schlumpf, the effects of the pion cloud were calculated through one-loop diagrams, including relativistic πNN vertex FFs. The model gives a relatively good global account of the data both at low Q^2 and larger Q^2 , though tends to show too much structure around the dipole form for the magnetic FFs at low Q^2 .

The cloudy bag model is one chiral quark model which treats the effect of pions perturbatively. Other quark models which calculated nucleon e.m. FFs using perturbative pions can be found e.g. in the early works of [?,156], as well as in the already discussed works of [142,143]. Recently,

the above chiral quark models where pions are included perturbatively have been improved in [157]. This work extends a previous work of [158] by dynamically dressing bare constituent quarks by mesons to fourth order within a manifestly Lorentz covariant formalism. Once the nucleon and Λ hyperon magnetic moments are fitted, other e.m. properties, such as the nucleon e.m. FFs at low momentum transfers, follow as a prediction. It was found in [157] that the meson cloud is able to nicely describe the FF data in the momentum transfer region up to about 0.5 GeV². To extend the calculations to larger Q^2 , a phenomenological approach has been adopted in [157] by introducing bare constituent quark FFs which were parameterized in terms of 10 parameters. Such parameterization makes it plausible to simultaneously explain the underlying dipole structure in the nucleon e.m. FF as well as the meson cloud contribution at low Q^2 which results from the underlying chiral dynamics. In a later paper [159], a model calculation for the bare constituent quark FFs has been performed and applied to the e.m. properties of the $N \rightarrow \Delta$ transition.

When pion effects dominate nucleon structure, their effects have to be treated non-perturbatively. A non-perturbative approach which has both quark and pion degrees of freedom and interpolates between a CQM and the Skyrme model (where the nucleon appears as a soliton solution of an effective nonlinear pion field theory) is the chiral quark soliton model (χ QSM). As for the Skyrme model, the χ QSM is based on a $1/N_c$ expansion (with N_c the number of colors in QCD). Its effective chiral action has been derived from the instanton model of the QCD vacuum [160], which provides a natural mechanism of chiral symmetry breaking and enables one to generate dynamically the constituent quark mass. Although in reality the number of colors N_c is equal to three, the extreme limit of large N_c is known to yield useful insights. At large N_c the nucleon is heavy and can be viewed as N_c “valence” quarks bound by a self-consistent pion field (the “soliton”) [161]. A successful description of static properties of baryons, such as mass splittings, axial constants, magnetic moments, FFs, has been achieved (typically at the 30 % level or better, see [162] for a review of early results). After reproducing masses and decay constants in the mesonic sector, the only free parameter left to be fixed in the baryonic sector is the constituent quark mass. When taking rotational ($1/N_c$) corrections into account, this model achieved a qualitative good description of the nucleon e.m. FFs in the range $Q^2 < 1$ GeV², using a constituent quark mass around 420 MeV [163]. The chiral soliton model naturally accounts for the decrease of the G_{Ep}/G_{Mp} ratio with increasing Q^2 . This can be understood from the hedgehog structure in soliton models which couples spatial rotations with isorotations. In the soliton rest frame, the isovector electric FF G_E^V therefore measures the rotational inertia density $\rho^V(r)$, in contrast to the isoscalar electric FF G_E^S which measures the isoscalar baryon density $\rho^S(r)$. For a rigid rotor, the inertia density is obtained from the baryon density as $\rho^V = r^2/r_B^2 \rho^S$, with r_B a free parameter characterizing the spatial extent.

Assuming a Gaussian density for $\rho^S(r)$, this yields [?] :

$$\frac{\mu_p G_{Ep}(Q^2)}{G_{Mp}(Q^2)} = 1 - \frac{1}{18} Q^2 r_B^2. \quad (38)$$

With the choice $r_B^2 \approx (0.3 \text{ fm})^2$, one can obtain an excellent fit of the polarization data for G_{Ep}/G_{Mp} . Although in the chiral soliton model calculation the baryon density is not exactly Gaussian, and the rigid rotor calculation does not hold exactly, these relations can be considered as approximate relations [?].

Holzwarth [?] extended the chiral soliton model by including the ρ (ω) meson propagators for the isovector (isoscalar) channels respectively. Furthermore, to extend the range in Q^2 of the predictions, he uses a relativistic prescription to boost the soliton rest frame densities to the Breit frame. Such prescription is also used to extract radial charge and magnetization rest frame densities from experimental FFs, as will be discussed in Sect. ?? . Using 4 fit parameters (one effective boost mass and three free parameters to fix the couplings of ρ and ω mesons), the model was found to provide a good account of the detailed structure of the nucleon e.m. FFs in the low Q^2 region. In particular, for G_{Ep}/G_{Mp} it predicts a decreasing ratio in good agreement with the data. At larger Q^2 , the boost prescription gives a reasonably good account of the data (except for G_{Mn}) and predicts a zero in G_{Ep} around 10 GeV^2 . Due to the uncertainty introduced from the particular choice for the boost prescription, the high Q^2 behavior (for Q^2 larger than about $4M^2$) of the e.m. FFs is however not a profound prediction of the low-energy effective model.

7.2 Dyson-Schwinger Equations and Diquark Models

The Dyson Schwinger equations (DSE) are generically a non-perturbative approximation for obtaining results for a field theory, in the present case QCD. The equations are, in principle, an infinite set of coupled integral equations. In practice, they must be truncated, in a way that preserves all symmetries of QCD, in order to proceed with any calculation. For a general DSE review, see [164].

One accomplishment of the DSE follows the solution for the full quark propagator, represented in momentum space as

$$S_F(p^2) = \frac{iF(p^2)}{\not{p} + M(p^2)}, \quad (39)$$

where the normalization $F(p^2)$ and the mass $M(p^2)$ become functions of momentum because of interactions. With relatively simple truncations and modeling of the QCD interactions, the DSE obtain a mass function in good agreement with lattice calculations. The mass $M(p^2)$ is several hundred MeV at small p^2 and falls smoothly to the small values at large p^2 that one might expect in perturbation theory.

Also early in the DSE program is building a model of the quark-quark and quark-antiquark interactions that will reproduce data on, among other quantities, the pion mass and decay constant.

One then uses the same quark-quark interactions developed in meson studies to obtain a three quark wave function model for the nucleon by solving the three-body Faddeev equations. There arise significant diquark, *i.e.*, significant quark-quark correlations, that have a strong effect on the form factors one obtains. Since the quarks in this model are dressed, many of their features are different from expectations for pointlike fermions. One finds in particular large quark anomalous chromomagnetic moments, which affect the quark-gluon interactions, which lead to large quark anomalous magnetic moments in the quark-photon interactions, which in turn are needed to obtain good fits to the nucleon electromagnetic form factor data.

The theoretical DSE results [165, 70, 166] show a falloff of the G_E^p/G_M^p ratio very similar to what is seen in the data 24.

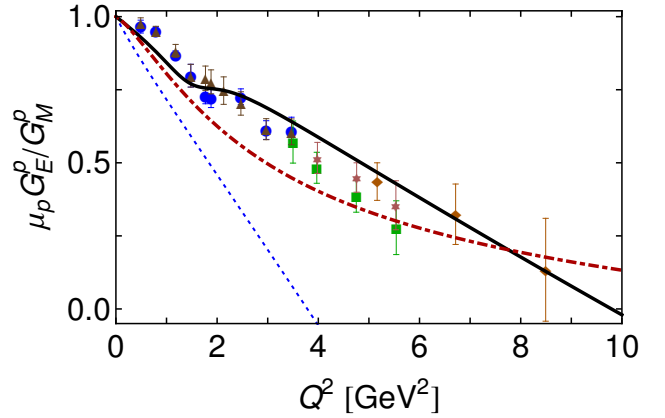


Fig. 24. Normalized G_E^p/G_M^p vs. Q^2 . The solid line is the DSE result from [167], the dash-dot line is the Kelly fit [121], and the dotted line is an earlier exploratory DSE result [168]. The data is from [27, 30, 28, 112, 101].

Qualitatively, the behavior of the form factors in the DSE approach is related to the behavior of the mass function $M(p^2)$. At lower momenta, where the mass function is far from its perturbative or current quark value, the Pauli form factor is also large compared to its perturbative value and is falling more slowly than perturbation theory predicts. (For reference, perturbative QCD predicts a Q^{-4} power law falloff for $F_1(Q^2)$ at large Q^2 , and a Q^{-6} falloff for $F_2(Q^2)$.) Hence one can get a zero in $G_E(Q^2)$,

$$G_E(Q^2) = F_1(Q^2) - \frac{Q^2}{4m_p^2} F_2(Q^2), \quad (40)$$

and hence a falloff in the ratio $G_E(Q^2)/G_M(Q^2)$.

For the newer DSE calculations [167], the zero in G_E is at $Q^2 = 9.5 \text{ GeV}^2$. If the mass function fell to its low perturbative value more quickly than it does, the quarks would behave more like free quarks, and the value of the Pauli or anomalous magnetic moment, form factor would be small as well as quickly falling. In such a case, the

zero of $G_F(Q^2)$ would be pushed to higher values of Q^2 or possibly not occur at all [167].

We may mention that models based on the Dyson-Schwinger equations do extend to form factors for other hadronic reactions, such as the electromagnetic $N \rightarrow \Delta$ transition [169,167]. The result for the ratio of the electric and magnetic transition form factors for this process, R_{EM} , turns out to be small in the DSE approach, even at momentum transfers above 5 GeV², in accord with experimental data. The perturbative QCD result, that $R_{EM} \rightarrow 1$ does ensue, but only at momentum transfers that are extremely high.

7.3 Links between Deep-Inelastic Scattering and Nucleon Form Factors

7.3.1 Perturbative QCD Inspired Models

Placeholder text

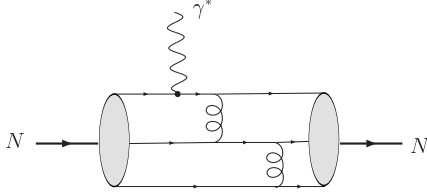


Fig. 25. Perturbative QCD picture for the nucleon e.m. FFs. The highly virtual photon resolves the leading three-quark Fock states of the nucleon, described by a distribution amplitude. The large momentum is transferred between the quarks through two successive gluon exchanges (only one of several possible lowest-order diagrams is shown).

The nucleon e.m. FFs provide a famous test for perturbative QCD. Brodsky and Farrar derived scaling rules for dominant helicity amplitudes which are expected to be valid at sufficiently high momentum transfers Q^2 [88]. A photon of sufficient high virtuality will see a nucleon consisting of three massless quarks moving collinear with the nucleon. When measuring an elastic nucleon FF, the final state consists again of three massless collinear quarks. In order for this (unlikely process) to happen, the large momentum of the virtual photon has to be transferred among the three quarks through two hard gluon exchanges as illustrated in 25. This hard scattering mechanism is generated by valence quark configurations with small transverse size and finite light-cone momentum fractions of the total hadron momentum carried by each valence quark. The hard amplitude can be written in a factorized form [?, ?, 170, 89], as a product of a perturbatively calculable hard scattering amplitude and two distribution amplitudes (DAs) describing how the large longitudinal momentum of the initial and final nucleons is shared between their constituents. Because each gluon in such hard scattering process carries a virtuality proportional to Q^2 , this leads to the pQCD prediction that the helicity conserving nucleon Dirac FF F_1 should fall as $1/Q^4$ (modulo $\ln Q^2$ factors) at

sufficiently high Q^2 . Processes such as in 25, where the interactions among the quarks proceed via gluon or photon exchange, both of which are vector interactions, conserve the quark helicity in the limit when the quark masses or off-shell effects can be neglected. In contrast to the helicity conserving FF F_1 , the nucleon Pauli FF F_2 involves a helicity flip between the initial and final nucleons. Hence it requires one helicity flip at the quark level, which is suppressed at large Q^2 . Therefore, for collinear quarks, i.e. moving in a light-cone WF state with orbital angular momentum projection $l_z = 0$ (along the direction of the fast moving hadron), the asymptotic prediction for F_2 leads to a $1/Q^6$ fall-off at high Q^2 .

We can test how well the above pQCD scaling predictions for the nucleon e.m. FFs are satisfied at currently available momentum transfers, see ???. One firstly sees that F_{1p} , which has been measured up to about 30 GeV², displays an approximate $1/Q^4$ scaling above 10 GeV². For the proton ratio F_{2p}/F_{1p} , the data up to 5.6 GeV² show no sign of a $1/Q^2$ behavior as predicted by pQCD. Instead, the data show that the ratio F_{2p}/F_{1p} falls less fast than $1/Q^2$ with increasing Q^2 . Belitsky, Ji, and Yuan [171] investigated the assumption of quarks moving collinearly with the proton, underlying the pQCD prediction. It has been shown in [171] that by including components in the nucleon light-cone WFs with quark orbital angular momentum projection $l_z = 1$, one obtains the behavior $F_2/F_1 \rightarrow \ln^2(Q^2/\Lambda^2)/Q^2$ at large Q^2 , with Λ a non-perturbative mass scale³. Choosing Λ around 0.3 GeV, Ref. [171] noticed that the data for F_{2p}/F_{1p} support such double-logarithmic enhancement, as can be seen from ??? (right panel). The arguments of [171] still rely on pQCD and it remains to be seen by forthcoming data at higher Q^2 if this prediction already starts in the few GeV² region.

Although at high enough Q^2 , the pQCD scaling predictions should set in, the available data for the nucleon e.m. FFs show that one is still far away from this regime. Nesterenko and Radyushkin [175] argued that the above described hard scattering mechanism is suppressed at accessible momentum transfers relative to the Feynman mechanism [176], also called soft mechanism. The soft mechanism involves only one active quark, and the FF is obtained as an overlap of initial and final hadron WFs. The hard scattering mechanism on the other hand, involving three active quarks, requires the exchange of two gluons, each of which brings in a suppression factor $\alpha_s/\pi \sim 0.1$. One therefore expects the hard scattering mechanism for F_{1p} to be numerically suppressed by a factor $1/100$ compared to the soft term, see also [177,178]. Even though the soft mechanism is suppressed asymptotically by a power of $1/Q^2$ relative to the hard scattering mechanism, it may well dominate at accessible values of Q^2 . In [175], the soft contribution to the nucleon e.m. FFs was estimated using a model based on local quark-hadron duality, and was found to yield an approximate $1/Q^4$ behavior in the range

³ In [86,172], it has also been discussed that inclusion of quark orbital angular momentum yields a ratio F_{2p}/F_{1p} which drops less fast than $1/Q^2$ with increasing Q^2 .

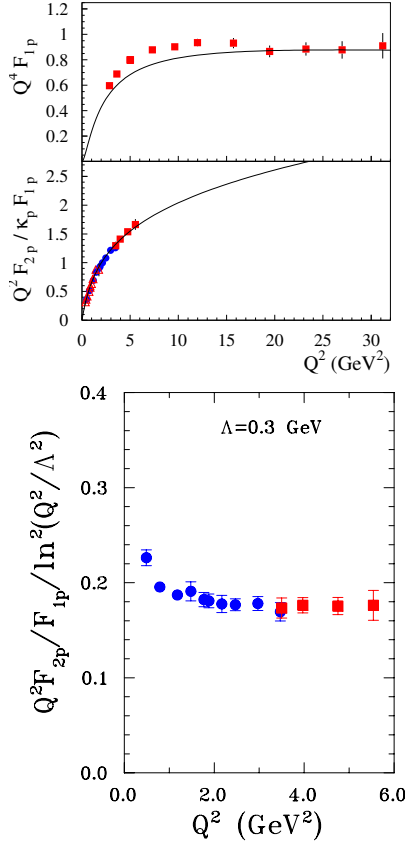


Fig. 26. Test of the scaling behavior of the proton FFs. Upper left panel : proton Dirac FF multiplied by Q^4 . Lower left panel : ratio of Pauli to Dirac proton FFs multiplied by Q^2 . Right panel : test of the modified scaling prediction for F_{2p}/F_{1p} of [171]. The data for F_{1p} are from [173] (solid squares). Data for the ratio F_{2p}/F_{1p} on both panels are from [?] (blue solid circles), [?] (red open triangles), and [?] (red solid squares). The curves on the left panels represent the calculation based on the three parameter modified Regge GPD parametrization of [174].

$Q^2 \sim 10 - 20 \text{ GeV}^2$, in qualitative agreement with the F_{1p} data.

In a more recent work, the soft contribution was evaluated within the light-cone sum rule (LCSR) approach [179]. Using asymptotic DAs for the nucleon, the LCSR approach yields values of G_{Mp} and G_{Mn} which are within 20 % compatible with the data in the range $Q^2 \sim 1 - 10 \text{ GeV}^2$. The electric FFs however were found to be much more difficult to describe, with G_{En} overestimated, and G_{Ep}/G_{Mp} near constant when using an asymptotic nucleon DA. Only when including twist-3 and twist-4 nucleon DAs within a simple model, is a qualitative description of the electric proton and neutron FFs obtained. Such higher twist components hint at the importance of quark angular momentum components in the nucleon WF.

In Sect. ??, we have shown that the nucleon e.m. FFs can be obtained from model independent GPD sum rules.

These GPDs, represented by the lower blob in 27, are non-perturbative objects which include higher Fock components in the nucleon WFs. One can use a GPD parametrization to provide an estimate of the soft contributions, and expects this non-perturbative approach to be relevant in the low and intermediate Q^2 region for the FFs. This is shown in ?? (solid curves) from which one sees that the GPD Regge parametrization discussed above is able to explain at the same time an approximate $1/Q^4$ behavior for F_{1p} and a behavior for F_{2p}/F_{1p} which falls less steep than $1/Q^2$. Forthcoming experiments at the Jefferson Lab 12 GeV facility will extend the data for F_{2p}/F_{1p} to Q^2 values around 13 GeV^2 . Such measurements will allow to quantify in detail the higher Fock components in the nucleon WF (which are all included in the nucleon GPD) versus the simple three-quark Fock component, and to map out the transition to the perturbative QCD regime.

7.3.2 Generalized Parton Distributions

Placeholder text

So far we have discussed the $N \rightarrow N$ transition as revealed with the help of the electromagnetic probe. By measuring the response of the hadron to a virtual photon, one measures the matrix element of a well-defined quark-gluon operator (in this case the vector operator $\bar{q}\gamma^\mu q$) over the hadronic state. This matrix element can be parametrized in terms of the nucleon e.m. FFs, revealing the quark-gluon structure of the nucleon. We are however not limited in nature to probes such as photons (or W , Z bosons for the axial transition). The phenomenon of asymptotic freedom of QCD, meaning that at short distances the interactions between quarks and gluons become weak, provides us with more sophisticated QCD operators to explore the structure of hadrons. Such operators can be accessed by selecting a small size configuration of quarks and gluons, provided by a hard reaction, such as deep inelastic scattering (DIS), or hard exclusive reactions such as deeply virtual Compton scattering (DVCS). We will be mostly interested here in DVCS reactions which are of the type $\gamma^*(q_h) + N(p) \rightarrow \gamma(q') + N(p')$, where the virtual photon momentum q_h is the hard scale. The common important feature of such hard reactions is the possibility to separate clearly the perturbative and nonperturbative stages of the interactions : this is the so-called factorization property.

The all-order factorization theorem for the DVCS process on the nucleon has been proven in [180–182]. Qualitatively one can say that the hard reactions allow one to perform a “microsurgery” of a nucleon by removing in a controlled way a quark of one flavor and spin and implanting instead another quark in the final nucleon. It is illustrated in 27 for the case of the DVCS process. The non-perturbative stage of such hard exclusive electroproduction processes is described by universal objects, so-called generalized parton distributions (GPDs) [183–185], see [186–190] for reviews and references.

The nucleon structure information entering the nucleon DVCS process, can be parametrized at leading twist-2 level, in terms of four quark chirality conserving GPDs.

The GPDs depend on three variables: the quark longitudinal momentum fractions x and ξ , and the momentum transfer $Q^2 = -q^2$ to the nucleon. The light-cone momentum fraction x is defined by $k^+ = xP^+$, where k is the quark loop momentum and P is the average nucleon momentum $P = (p + p')/2$, where $p(p')$ are the initial (final) nucleon four-momenta respectively, see 27. The skewedness variable ξ is defined by $q^+ = -2\xi P^+$, where $q = p' - p$ is the overall momentum transfer in the process, and where $2\xi \rightarrow x_B/(1 - x_B/2)$ in the Bjorken limit: $x_B = Q_h^2/(2p \cdot q_h)$ is the usual Bjorken scaling variable, with $Q_h^2 = -q_h^2 > 0$ the virtuality of the hard photon.

The DVCS process corresponds to the kinematics $Q_h^2 \gg Q^2, M^2$, so that at twist-2 level, terms proportional to Q^2/Q_h^2 or M^2/Q_h^2 are neglected in the amplitude. In a frame where the virtual photon momentum q_h^μ and the average nucleon momentum P^μ are collinear along the z -axis and in opposite directions, one can parameterize the non-perturbative object entering the nucleon DVCS process as (following Ji [184])⁴:

$$\begin{aligned} & \frac{1}{2\pi} \int dy^- e^{ixP^+ y^-} \\ & \times \langle N(p') | \bar{\psi}(-y/2) \gamma \cdot n \psi(y/2) | N(p) \rangle \Big|_{y^+ = y_\perp = 0} \\ & = H^q(x, \xi, Q^2) \bar{N}(p') \gamma \cdot n N(p) \\ & + E^q(x, \xi, Q^2) \bar{N}(p') i\sigma^{\mu\nu} \frac{n_\mu q_\nu}{2M} N(p), \end{aligned} \quad (41)$$

where ψ is the quark field of flavor q , N the nucleon spinor, and n^μ is a light-cone vector along the negative z -direction. The *lhs* of Eq. (41) can be interpreted as a Fourier integral along the light-cone distance y^- of a quark-quark correlation function, representing the process where a quark is taken out of the initial nucleon (having momentum p) at the space-time point $y/2$, and is put back in the final nucleon (having momentum p') at the space-time point $-y/2$. This process takes place at equal light-cone time ($y^+ = 0$) and at zero transverse separation ($y_\perp = 0$) between the quarks. The resulting one-dimensional Fourier integral along the light-cone distance y^- is with respect to the quark light-cone momentum xP^+ . The *rhs* of Eq. (41) parametrizes this non-perturbative object in terms of the GPDs H^q and E^q for a quark of flavor q . The quark vector operator ($\gamma \cdot n$) corresponds at the nucleon side to a vector transition (parametrized by the function H^q) and a tensor transition (parametrized by the function E^q). Analogously, there are two GPDs corresponding to a quark axial vector operator ($\gamma \cdot n \gamma_5$), which are commonly denoted by the polarized GPDs \tilde{H}^q and \tilde{E}^q .

The variable x in the GPDs runs from -1 to 1 . Therefore, the momentum fractions of the active quarks ($x + \xi$) for the initial quark and ($x - \xi$) for the final quark can either be positive or negative. Since positive (negative) momentum fractions correspond to quarks (antiquarks), it has been noted in [185] that in this way, one can iden-

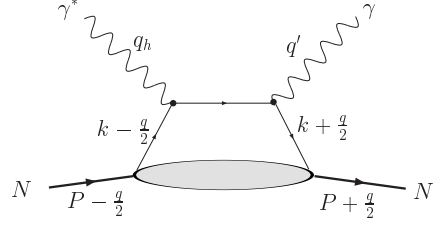


Fig. 27. The “handbag” diagram for the nucleon DVCS process. Provided the virtuality of the initial photon (with momentum q_h) is sufficiently large, the QCD factorization theorem allows to express the total amplitude as the convolution of a Compton process at the quark level and a non-perturbative amplitude parameterized in terms of generalized parton distributions (lower blob). The diagram with the photon lines crossed is also understood.

tify two regions for the GPDs: when $x > \xi$ both partons represent quarks, whereas for $x < -\xi$ both partons represent antiquarks. In these regions, the GPDs are the generalizations of the usual parton distributions from DIS. Actually, in the forward direction, the GPD H reduces to the quark (anti-quark) density distribution $q(x)$ ($\bar{q}(x)$) obtained from DIS: $H^q(x, 0, 0) = q(x)$, for $x > 0$; $H^q(x, 0, 0) = -\bar{q}(-x)$, for $x < 0$. The GPD E is not measurable through DIS because the associated tensor in Eq. (41) vanishes in the forward limit ($q \rightarrow 0$). Therefore, E is a new leading twist function, which is accessible by measuring hard exclusive electroproduction reactions, such as DVCS.

Besides coinciding with the quark distributions at vanishing momentum transfer, the GPDs have interesting links with other nucleon structure quantities. The first moments of the GPDs are related to the elastic FFs of the nucleon through model independent sum rules. By integrating Eq. (41) over x , one obtains for any ξ the following relations for a particular quark flavor [184] :

$$\begin{aligned} & \int_{-1}^{+1} dx H^q(x, \xi, Q^2) = F_1^q(Q^2), \\ & \int_{-1}^{+1} dx E^q(x, \xi, Q^2) = F_2^q(Q^2), \end{aligned} \quad (42)$$

where F_1^q (F_2^q) represents the elastic Dirac (Pauli) FFs for the quark flavor q in the nucleon. These quark FFs are expressed, using $SU(2)$ isospin, as flavor combinations of the proton and neutron elastic FFs as:

$$\begin{aligned} F_1^u &= 2 F_{1p} + F_{1n} + F_1^s, \\ F_1^d &= 2 F_{1n} + F_{1p} + F_1^s, \end{aligned} \quad (43)$$

where F_1^s is the strangeness FF of the nucleon (which is neglected in the calculations discussed below). Relations similar to Eq. (43) hold for the Pauli FFs F_2^q . At $Q^2 = 0$, the normalizations of the Dirac FFs are given by: $F_1^u(0) = 2$ ($F_1^d(0) = 1$) so as to yield the normalization of 2 (1) for the u (d)-quark distributions in the proton. The normalizations of the Pauli FF at $Q^2 = 0$ are given by $F_2^q(0) = \kappa^q$ (for $q = u, d$), where κ^u, κ^d can be expressed

⁴ In all non-local expressions we always assume the gauge link: $P \exp(i g \int dx^\mu A_\mu)$, ensuring the color gauge invariance.

in terms of the proton (κ_p) and neutron (κ_n) anomalous magnetic moments as:

$$\begin{aligned}\kappa^u &\equiv 2\kappa_p + \kappa_n = +1.673, \\ \kappa^d &\equiv \kappa_p + 2\kappa_n = -2.033.\end{aligned}\quad (44)$$

The above sum rules allow us to make a prediction for the nucleon e.m. FFs provided we have a model for the nucleon GPDs. Note that the sum rules of Eq. (42) only involve valence quark GPDs, since the sea-quark and anti-quark contributions cancel each other in the sum rules. Since the results of the integration in Eq. (42) do not depend on the skewness ξ ⁵, one can choose $\xi = 0$ in these sum rules. We therefore only discuss the GPDs H and E at $\xi = 0$ in the following.

In [191,174], parameterizations of GPDs were developed which have a Regge behavior at small x and Q^2 , and which were modified to larger Q^2 behavior so as to lead to the observed power behavior of the FFs [192,193]. A modified Regge parameterization for H and E was proposed in [174]:

$$\begin{aligned}H^q(x, 0, Q^2) &= q_v(x) x^{\alpha' (1-x) Q^2}, \\ E^q(x, 0, Q^2) &= \frac{\kappa^q}{N^q} (1-x)^{\eta^q} q_v(x) x^{\alpha' (1-x) Q^2},\end{aligned}\quad (45)$$

depending on 3 parameters. The Regge slope α' is determined from the Dirac radius, and two parameters η^u and η^d , entering the GPD E , ensure that the $x \sim 1$ limit of E^q has extra powers of $1-x$ compared to that of H^q . This results in a proton helicity flip FF F_2 which has a faster power fall-off at large Q^2 than F_1 , as observed experimentally. Furthermore, in Eq. (45), the normalization factors N^u and N^d are given by:

$$\begin{aligned}N^u &= \int_0^1 dx (1-x)^{\eta^u} u_v(x), \\ N^d &= \int_0^1 dx (1-x)^{\eta^d} d_v(x),\end{aligned}\quad (46)$$

and guarantee the normalization condition for the GPD E^q . Diehl *et al.* [191] chose a more general functional form for E^q at the expense of more free parameters. In the following, we discuss the ‘minimal’ model with 3 parameters, and refer the interested reader to [191] for a study of more general functional forms. The 3 free parameters in the resulting modified Regge ansatz are to be determined from a fit to the FF data.

In Fig. 28, the proton and neutron Sachs electric and magnetic FFs are shown. One observes that the 3-parameter modified Regge model gives a rather good overall description of the available FF data for both proton and neutron in the whole Q^2 range, using as value for the Regge trajectory $\alpha' = 1.105 \text{ GeV}^{-2}$, and the following values for the coefficients governing the $x \rightarrow 1$ behavior of the E -type GPDs: $\eta^u = 1.713$ and $\eta^d = 0.566$. Note that a value $\eta^q = 2$ corresponds to a $1/Q^2$ asymptotic behavior of the

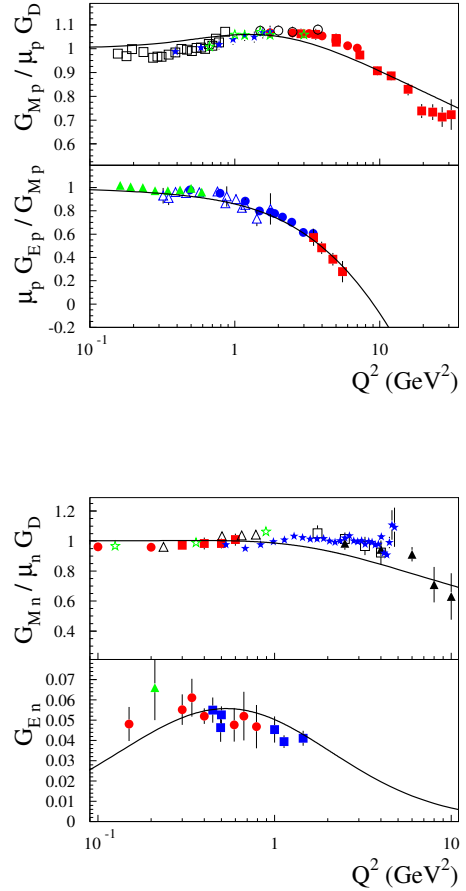


Fig. 28. GPD calculation of G_{Mp} and G_{Mn} relative to the dipole G_D (upper panels), ratio of G_{Ep}/G_{Mp} (lower left panel), and G_{En} (lower right panel), according to Ref. [174]. The curves are a 3 parameter modified Regge parameterization: $\alpha' = 1.105 \text{ GeV}^{-2}$, $\eta^u = 1.713$ and $\eta^d = 0.566$. Data for G_{Mp} are from [194] (open squares), [26] (open circles), [107] (blue solid stars), [108] (green open stars), [?] (red solid circles), [173] (red solid squares), according to the recent re-analysis of Ref. [195]. Data for the ratio G_{Ep}/G_{Mp} are from [?] (blue open triangles), [?] (red solid squares), [?] (blue solid circles), and [106] (green solid triangles). The data for G_{Mn} are from [196] (red solid circles), [197] (red solid squares), [198] (open triangles), [122] (green open stars), [199] (open squares), [?] (solid triangles), and [?] (blue solid stars). The data for G_{En} are from double polarization experiments at MAMI [16,17,78,79,200] (red solid circles), NIKHEF [15] (green solid triangle), and JLab [72,84,73] (blue solid squares).

ratio F_2^q/F_1^q at large Q^2 . The modified Regge GPD parameterization allows to accurately describe the decreasing ratio of G_{Ep}/G_{Mp} with increasing Q^2 , and also leads to a zero for G_{Ep} at a momentum transfer of $Q^2 \simeq 8 \text{ GeV}^2$, which will be within the range covered by an upcoming JLab experiment [201].

⁵ This is the simplest example of a so-called polynomiality condition when calculating moments of GPDs.

7.4 Lattice QCD Calculations of Nucleon Form Factors

Strictly speaking, lattice calculations of nucleon form factors are currently available only for the isovector form factors.

Isoscalar form factors require calculations of disconnected diagrams, which are diagrams with quark loops not connected to the quark lines emanating from or ending on the lattice nucleon source or sink. There are gluons that attach the quark loops to the valence quarks, but these are not indicated in lattice diagrams, hence the phrase “disconnected.” Contributions from the disconnected loops require computer time intensive calculations, and the calculations remain undone. However, the disconnected diagrams contribute equally to proton and neutron, so the isovector case can be considered without them.

A review including lattice form factor results up to 2010 is available in [202], and newer lattice form factor results are reported in [203–205].

The new calculations have pion masses from 373 MeV down to a close to physical 149 MeV in [205]. The latter also strove to reduce contamination from excited nucleons. They analyze their lattice data using three methods which they call the standard ratio method, the summation method, and the generalized pencil-of-function method (GPoF), with varying outcomes. The best results, judged by comparison to data as represented by one of the standard fits [206], come from the summation method. Here agreement with experimental data is good for both G_E^v and G_M^v in the region considered, which is Q^2 from scattering threshold up to about 0.5 GeV², with uncertainty limits about 20% at Q^2 of 0.4 GeV²,

Refs. [203,204] have pion masses in the 213–373 MeV range, and quote results for somewhat higher Q^2 . For Q^2 above about 0.6 GeV², their isovector form factors results tend to be 50% or so above the data for G_E^v (or F_1^v), with uncertainties indicated at about 10%. For G_M^v (or F_2^v) the results are closer to data. The authors of these works do point out that the lattice treatments with these pion masses are all consistent with each other.

One may specifically focus on nucleon radii calculated from lattice gauge theory. In the future, it may be possible and desirable to calculate using a dedicated correlator which gives directly the slope of the form factor at zero momentum transfer. Finding such correlators by taking derivatives of known correlators is suggested and studied [207] for lattice calculations of form factors at points where the Lorentz factors they multiply go to zero. Applications in [207] are to form factors for semi-leptonic scalar meson decay, and to hadronic vacuum polarization corrections to the muon ($g - 2$).

At present, lattice calculations of nucleon radii proceed by calculating the form factor at several non-zero Q^2 , fitting to a suitable form, typically a dipole form, and finding the radius by extrapolating to zero Q^2 . Truly complete results are available only for the isovector nucleon. Ref. [205] presents a plot of radius results for lattice calculations at various pion masses. They use the Dirac radius, obtained from the slope of F_1^v , rather than the charge radius, but

these are related by, using the proton as an example,

$$\langle r_{1p}^2 \rangle = \langle r_{Ep}^2 \rangle - \frac{3}{2} \frac{\kappa_p}{m_p^2}. \quad (47)$$

Hence, given the great accuracy of the magnetic moment measurements, one knows the Dirac radii to the same accuracy as the charge radii.

The great interest is obtain sufficient accuracy from the lattice results to be able to adjudicate between the electron and muon measured values of the isovector charge or Dirac radii. The electron measured isovector radius is straightforward to look up, the muon measured value of the Dirac or charge radius is for now a defined quantity obtained by using the electron value for the neutron radius-squared. Using the summation method, Ref. [205] obtain, by extrapolation to the physical pion mass, a value of the isovector Dirac radius between the muonic and electronic results, with uncertainties that accommodate both at about the one standard deviation level. However, using the GPoF or ratio method gives a smaller $\langle r_1^2 \rangle^v$, on the order of 2/3 the value from the summation method.

One may say there opportunity for further work. An uncertainty of 1% or less for the proton alone is needed for a lattice calculation to impact the proton radius puzzle.

References

1. M.N. Rosenbluth, Phys. Rev. **79**, 615 (1950)
2. R. Hofstadter, Rev. Mod. Phys. **28**, 214 (1956)
3. D.R. Yennie, M.M. Lévy, D.G. Ravenhall, Rev. Mod. Phys. **29**, 144 (1957)
4. R. Hofstadter, H. Fechter, J. McIntyre, Phys. Rev. **92**, 978 (1953)
5. A.I. Akhiezer, M.P. Rekalo, Sov. Phys. Dokl. **13**, 572 (1968)
6. A.I. Akhiezer, M.P. Rekalo, Dokl. Akad. Nauk Ser. Fiz. **180**, 1081 (1968)
7. A.I. Akhiezer, M.P. Rekalo, Sov. J. Part. Nucl. **4**, 277 (1974)
8. A.I. Akhiezer, M.P. Rekalo, Fiz. Elem. Chast. Atom. Yadra **4**, 662 (1973)
9. N. Dombey, Rev. Mod. Phys. **41**, 236 (1969)
10. R.G. Arnold, C.E. Carlson, F. Gross, Phys. Rev. C **23**, 363 (1981)
11. S. Riordan, S. Abrahamyan, B. Craver, A. Kelleher, A. Kolarkar et al., Phys.Rev.Lett. **105**, 262302 (2010), 1008.1738
12. P. Dolph, J. Singh, T. Averett, A. Kelleher, K. Mooney et al., Phys.Rev. **C84**, 065201 (2011), 1107.1902
13. J. Bizot, Phys.Rev. **B140**, 1387 (1965)
14. T. Powell, M. Borghini, O. Chamberlain, R.Z. Fuzesy, C.C. Morehouse et al., Phys.Rev.Lett. **24**, 753 (1970)
15. I. Passchier et al., Phys. Rev. Lett. **82**, 4988 (1999)
16. C. Herberg et al., Eur. Phys. J. A **5**, 131 (1999)
17. M. Ostrick et al., Eur. Phys. J. A **83**, 276 (1999)
18. D. Eyl, A. Frey, H. Andresen, J. Annand, K. Aulenbacher et al., Z.Phys. **A352**, 211 (1995)
19. Th. Pospischil et al., Eur. Phys. J. A **12**, 125 (2001)
20. T. Eden, R. Madey, W. Zhang, B. Anderson, H. Arenhovel et al., Phys.Rev. **C50**, 1749 (1994)

21. D. Barkhuff *et al.*, Phys. Lett. **470**, 39 (1999)
22. B.D. Milbrath *et al.*, Bates FPP collaboration, Phys. Rev. Lett. **80**, 452 (1998)
23. B.D. Milbrath *et al.*, Bates FPP collaboration, Phys. Rev. Lett. **82**, 2221 (erratum) (1999)
24. E. Beise, M. Pitt, D. Spayde, Prog.Part.Nucl.Phys. **54**, 289 (2005), [nucl-ex/0412054](#)
25. I.A. Qattan, *et al.*, Phys. Rev. Lett. **94**, 142301 (2005)
26. J. Litt *et al.*, Phys. Lett. B **31**, 40 (1970)
27. M.K. Jones *et al.*, Jefferson Lab Hall A Collaboration, Phys. Rev. Lett. **84**, 1398 (2000)
28. V. Punjabi *et al.*, Phys. Rev. C **71**, 055202 (2005)
29. V. Punjabi *et al.*, Phys. Rev. C **71**, 069902 (2005)
30. O. Gayou *et al.*, Jefferson Lab Hall A Collaboration, Phys. Rev. Lett. **88**, 092301 (2002)
31. I. Sick, Phys.Lett. **B576**, 62 (2003), [nucl-ex/0310008](#)
32. I. Sick, D. Trautmann, Phys.Rev. **C89**(1), 012201 (2014), [1407.1676](#)
33. K. Melnikov, T. van Ritbergen, Phys.Rev.Lett. **84**, 1673 (2000), [hep-ph/9911277](#)
34. A. Antognini, F. Kottmann, F. Biraben, P. Indelicato, F. Nez *et al.*, Annals Phys. **331**, 127 (2013), [1208.2637](#)
35. R. Pohl, R. Gilman, G.A. Miller, K. Pachucki, Ann.Rev.Nucl.Part.Sci. **63**, 175 (2013), [1301.0905](#)
36. T.W. Donnelly, A.S. Raskin, Ann. Phys. **169**, 247 (1986)
37. A.S. Raskin, T.W. Donnelly, Ann. Phys. **191**, 78 (1986)
38. M. Diehl, P. Kroll, Eur.Phys.J. **C73**, 2397 (2013), [1302.4604](#)
39. P.A.M. Guichon, M. Vanderhaeghen, Phys. Rev. Lett. **91**, 142303 (2003)
40. A.V. Afanasev, S.J. Brodsky, C.E. Carlson, Y.C. Chen, M. Vanderhaeghen, Phys. Rev. D **72**, 013008 (2005)
41. N. Kivel, M. Vanderhaeghen, JHEP **1304**, 029 (2013), [1212.0683](#)
42. H.Y. Gao, Int. J. Mod. Phys. E **12**, 1 (2003)
43. H.Y. Gao, Int. J. Mod. Phys. E **12**, 567 (2003)
44. C.E. Hyde-Wright, K. de Jager, Ann. Rev. Nucl. Part. Sci. **54**, 217 (2004)
45. C. Perdrisat, V. Punjabi, M. Vanderhaeghen, Prog.Part.Nucl.Phys. **59**, 694 (2007), [hep-ph/0612014](#)
46. J. Arrington, C.D. Roberts, J.M. Zanotti, J. Phys. G p. 34 (2006)
47. J. Arrington, K. de Jager, C.F. Perdrisat, J.Phys.Conf.Ser. **299**, 012002 (2011), [1102.2463](#)
48. I. Cloët, G. Eichmann, B. El-Bennich, T. Klahn, C. Roberts, Few Body Syst. **46**, 1 (2009), [0812.0416](#)
49. C. Perdrisat, V. Punjabi, **5(8)**, 10204 (2010), [1410.6626](#)
50. O. Gayou *et al.*, Phys. Rev. Lett. **64**, 038202 (2001)
51. B. Anderson *et al.*, Jefferson Lab E95-001 Collaboration, Phys. Rev. C **75**, 034003 (2007)
52. W.K. Brooks, J.D. Lachniet, CLAS Collaboration, Nucl. Phys. A **755**, 261 (2005)
53. J. Lachniet, Ph.D. thesis, Carnegie Mellon Univesity (2005)
54. F. Iachello, A.D. Jackson, A. Landé, Phys. Lett. B **43**, 191 (1973)
55. G. Höhler *et al.*, Nucl. Phys. B **114**, 505 (1976)
56. M.F. Gari, W. Krümpelmann, Z. Phys. A **322**, 689 (1985)
57. M.F. Gari, W. Krümpelmann, Phys. Lett. B **274**, 150 (1992)
58. M.E. Christy *et al.*, Phys. Rev. C **70**, 015206 (2004)
59. E. Lomon, Phys. Rev. C **64**, 035204 (2001)
60. R. Bijker, F. Iachello, Phys. Rev. C **69**, 068201 (2004)
61. R.R. Wilson, J.S. Levinger, Ann. Rev. Nucl. Part. Sci. **14**, 135 (1964),
62. G.A. Miller, Phys. Rev. C **68**, 022201(R) (2003)
63. C.E. Carlson, M. Vanderhaeghen, Phys.Rev.Lett. **100**, 032004 (2008), [0710.0835](#)
64. I. Cloet, C. Roberts, PoS **LC2008**, 047 (2008), [0811.2018](#)
65. M. Galynskii, E. Kuraev, Phys.Rev. **D89**(5), 054005 (2014), [1312.3742](#)
66. I.C. Cloet, G.A. Miller, Phys.Rev. **C86**, 015208 (2012), [1204.4422](#)
67. G. Cates, C. de Jager, S. Riordan, B. Wojtsekhowski, Phys.Rev.Lett. **106**, 252003 (2011), [1103.1808](#)
68. M. Rohrmoser, K.S. Choi, W. Plessas (2011), [1110.3665](#)
69. D. Wilson, I. Cloet, L. Chang, C. Roberts, Phys.Rev. **C85**, 025205 (2012), [1112.2212](#)
70. I.C. Cloët, C.D. Roberts, A.W. Thomas, Phys.Rev.Lett. **111**, 101803 (2013), [1304.0855](#)
71. I. Qattan, J. Arrington (2013), [1307.7388](#)
72. H. Zhu *et al.*, Phys. Rev. Lett. **87**, 081801 (2001)
73. G. Warren *et al.*, Jefferson Lab E93-026 Collaboration, Phys. Rev. Lett. **92**, 042301 (2004)
74. E. Geis *et al.* (BLAST Collaboration), Phys.Rev.Lett. **101**, 042501 (2008), [0803.3827](#)
75. C.E. Jones-Woodward *et al.*, Phys. Rev. C **44**, 571 (1991)
76. A.K. Thompson *et al.*, Phys. Rev. Lett. **68**, 2901 (1992)
77. M. Meyerhoff, D. Eyl, A. Frey, H. Andresen, J. Annand *et al.*, Phys.Lett. **B327**, 201 (1994)
78. J. Becker *et al.*, Eur. Phys. J. A **6**, 329 (1999)
79. D. Rohe *et al.*, Phys. Rev. Lett. **83**, 4257 (1999)
80. J. Bermuth *et al.*, Phys. Lett. B **564**, 199 (2003)
81. J. Golak, G. Ziemer, H. Kamada, H. Witala, W. Gloeckle, Phys.Rev. **C63**, 034006 (2001), [nucl-th/0008008](#)
82. B. Schlimme, P. Achenbach, C. Ayerbe Gayoso, J. Bernauer, R. Bhm *et al.*, Phys.Rev.Lett. **111**(13), 132504 (2013), [1307.7361](#)
83. D. Glazier, M. Seimetz, J. Annand, H. Arenhovel, M. Ases Antelo *et al.*, Eur.Phys.J. **A24**, 101 (2005), [nucl-ex/0410026](#)
84. R. Madey *et al.*, E93-038 Collaboration, Phys. Rev. Lett. **91**, 122002 (2003)
85. B. Plaster *et al.*, Phys. Rev. C **73**, 025205 (2006)
86. J.P. Ralston, P. Jain, Phys.Rev. D **69**, 053008 (2004)
87. A.V. Belitsky, X.d. Ji, F. Yuan, Phys.Rev.Lett. **91**, 092003 (2003), [hep-ph/0212351](#)
88. S.J. Brodsky, G.R. Farrar, Phys. Rev. D **11**, 1309 (1975)
89. G.P. Lepage, S.J. Brodsky, Phys. Rev. D **22**, 2157 (1980)
90. L. Andivahis *et al.*, Phys. Rev. D **50**, 5491 (1994)
91. P.E. Bosted *et al.*, Phys. Rev. Lett. **68**, 3841 (1992)
92. S. Brodsky, pp. 1–33 (2002), [hep-ph/0208158](#)
93. J.P. Ralston, P. Jain, R.V. Buniy, AIP Conf.Proc. **549**, 302 (2000), [hep-ph/0206074](#)
94. G.A. Miller, M.R. Frank, Phys. Rev. C **65**, 065205 (2002)
95. M.J. Alguard *et al.*, Phys. Rev. Lett. **37**, 1258 (1976)
96. S. Dietrich *et al.*, Phys. Lett. B **500**, 47 (2001)
97. S. Strauch *et al.*, Phys. Rev. Lett. **91**, 052301 (2003)
98. B. Hu *et al.*, Phys. Rev. C **73**, 064004 (2006)
99. G. MacLachlan *et al.*, Nucl. Phys. A **764**, 261 (2006)
100. J. Alcorn *et al.*, Nucl. Instrum. Meth. A **522**, 294 (2004)
101. A. Puckett, E. Brash, O. Gayou, M. Jones, L. Pentchev *et al.*, Phys.Rev. **C85**, 045203 (2012), [1102.5737](#)
102. H. Spinka *et al.*, Nucl. Instrum. Meth. **211**, 239 (1983)
103. D. Miller *et al.*, Phys. Rev. D **16**, 2016 (1977)

104. N.E. Cheung *et al.*, Nucl. Instrum. Meth. A **363**, 561 (1995)
105. M.K. Jones *et al.*, Jefferson Lab Resonance Spin Structure Collaboration, Phys. Rev. C **74**, 035201 (2006)
106. C.B. Crawford *et al.*, Phys. Rev. Lett. **98**, 052301 (2007)
107. Ch. Berger *et al.*, Phys. Lett. B **35**, 87 (1971)
108. W. Bartel *et al.*, Nucl. Phys. B **58**, 429 (1973)
109. L.E. Price *et al.*, Phys. Rev. D **4**, 45 (1971)
110. K.M. Hanson *et al.*, Phys. Rev. D **8**, 753 (1973)
111. J. Arrington, Phys. Rev. C **68**, 034325 (2003)
112. A. Puckett, E. Brash, M. Jones, W. Luo, M. Mezziane *et al.*, Phys.Rev.Lett. **104**, 242301 (2010), 1005.3419
113. M. Paolone, S. Malace, S. Strauch, I. Albayrak, J. Arrington *et al.*, Phys.Rev.Lett. **105**, 072001 (2010), 1002.2188
114. M. Mezziane *et al.* (GEP2gamma Collaboration), Phys.Rev.Lett. **106**, 132501 (2011), 1012.0339
115. C.G. Boyd, B. Grinstein, R.F. Lebed, Nucl.Phys. **B461**, 493 (1996), hep-ph/9508211
116. C. Bourrely, I. Caprini, L. Lellouch, Phys.Rev. **D79**, 013008 (2009), 0807.2722
117. R.J. Hill, G. Paz, Phys.Rev. **D82**, 113005 (2010), 1008.4619
118. I. Lorenz, U.G. Meißner, Phys.Lett. **B737**, 57 (2014), 1406.2962
119. J. Bernauer *et al.* (A1 Collaboration), Phys.Rev.Lett. **105**, 242001 (2010), 1007.5076
120. I. Lorenz, U.G. Meißner, H.W. Hammer, Y.B. Dong (2014), 1411.1704
121. J. J. Kelly, Phys. Rev. C **70**, 068202 (2004)
122. G. Kubon *et al.*, Phys. Lett. B **524**, 26 (2002)
123. I. Lorenz, H.W. Hammer, U.G. Meissner, Eur.Phys.J. **A48**, 151 (2012), 1205.6628
124. R. Baldini, C. Bini, P. Gauzzi, M. Mirazita, M. Negrini *et al.*, Eur.Phys.J. **C46**, 421 (2006), hep-ph/0507085
125. M.A. Belushkin, H.W. Hammer, U.G. Meissner, Phys. Rev. C **75**, 035202 (2007)
126. R. Baldini Ferroli, S. Pacetti, Nucl.Phys.Proc.Suppl. **225-227**, 211 (2012)
127. S.J. Brodsky, C.E. Carlson, J.R. Hiller, D.S. Hwang, Phys.Rev. **D69**, 054022 (2004), hep-ph/0310277
128. A. De Rujula, H. Georgi, S.L. Glashow, Phys. Rev. D **12**, 147 (1975)
129. N. Isgur, G. Karl, R. Koniuk, Phys. Rev. D **25**, 2394 (1982)
130. S.L. Glashow, Physica **96A**, 27 (1979)
131. V. Pascalutsa, M. Vanderhaeghen, S.N. Yang, Phys. Rept. **437**, 125 (2007)
132. P.A.M. Dirac, Rev. Mod. Phys. **21**, 392 (1949)
133. P.L. Chung, F. Coester, Phys. Rev. D **44**, 229 (1991)
134. H.J. Melosh, Phys. Rev. D **9**, 1095 (1974)
135. M.R. Frank, B.K. Jennings, G.A. Miller, Phys. Rev. C **54**, 920 (1996)
136. F. Cardarelli, E. Paceand G. Salme, S. Simula, Phys. Lett. B **357**, 267 (1995)
137. F. Cardarelli, S. Simula, Phys. Rev. C **62**, 65201 (2000)
138. S. Boffi, L.Y. Glozman, W. Klink, W. Plessas, M. Radici, R.F. Wagenbrunn, Eur. Phys. J. A **14**, 17 (2002)
139. F. Gross, P. Agbakpe, Phys. Rev. C **73**, 015203 (2006)
140. S. Capstick, N. Isgur, Phys. Rev. D **34**, 2809 (1986)
141. E. Pace, G. Salme, F. Cardarelli, S. Simula, Nucl. Phys. A **666and667**, 33c (2000)
142. L.Y. Glozman, Z. Papp, W. Plessas, K. Varga, R.F. Wagenbrunn, Phys. Rev. C **57**, 3406 (1998)
143. L.Y. Glozman, W. Plessas, K. Varga, R.F. Wagenbrunn, Phys. Rev. D **58**, 094030 (1998)
144. R.F. Wagenbrunn, S. Boffi, W. Klink, W. Plessas, M. Radici, Phys. Lett. B **511**, 33 (2001)
145. R. Wagenbrunn, T. Melde, W. Plessas (2005), hep-ph/0509047
146. F. Coester, D.O. Riska, Nucl. Phys. A **728**, 439 (2003)
147. B. Julia-Diaz, D.O. Riska, F. Coester, Phys. Rev. C **69**, 035212 (2004)
148. D. Merten, U. Loring, K. Kretzschmar, B. Metsch, H.R. Petry, Eur. Phys. J. A **14**, 477 (2002)
149. B. Desplanques, L. Theussl, Eur. Phys. J. A **21**, 93 (2004)
150. B. Desplanques (2005), nucl-th/0510003
151. M. De Sanctis, M.M. Giannini, L. Repetto, E. Santopinto, Phys. Rev. C **62**, 025208 (2000)
152. A. Manohar, H. Georgi, Nucl. Phys. B **234**, 189 (1984)
153. A.W. Thomas, Adv. Nucl. Phys. **13**, 1 (1984)
154. D.H. Lu, A.W. Thomas, A.G. Williams, Phys. Rev. C **57**, 2628 (1998)
155. G.A. Miller, Phys. Rev. C **66**, 032201(R) (2002)
156. S.N. Jena, S. Panda, J. Phys. G **18**, 273 (1992)
157. A. Faessler, T. Gutsche, V.E. Lyubovitskij, K. Pumsaard, Phys. Rev. D **73**, 114021 (2006)
158. V.E. Lyubovitskij, T. Gutsche, A. Faessler, Phys. Rev. C **64**, 065203 (2001)
159. A. Faessler, T. Gutsche, B. R. Holstein, V. E. Lyubovitskij, D. Nicmorus, K. Pumsaard, Phys. Rev. D **74**, 074010 (2006)
160. D.I. Diakonov, V. Petrov, Nucl. Phys. B **272**, 457 (1986)
161. D.I. Diakonov, V. Petrov, P. Pobylitsa, Nucl. Phys. B **306**, 809 (1988)
162. Chr.V. Christov, A. Blotz, H.C. Kim, P. Pobylitsa, T. Watabe, Th. Meissner, E. Ruiz Arriola, K. Goeke, Prog. Part. Nucl. Phys. **37**, 91 (1996)
163. C.V. Christov, A.Z. Gorski, K. Goeke, P.V. Pobylitsa, Nucl. Phys. A **592**, 513 (1995)
164. A. Bashir, L. Chang, I.C. Cloet, B. El-Bennich, Y.X. Liu *et al.*, Commun.Theor.Phys. **58**, 79 (2012), 1201.3366
165. I.C. Cloët, W. Bentz, A.W. Thomas, Phys.Rev. **C90**, 045202 (2014), 1405.5542
166. I.C. Cloët, C.D. Roberts, Prog.Part.Nucl.Phys. **77**, 1 (2014), 1310.2651
167. J. Segovia, I.C. Cloët, C.D. Roberts, S.M. Schmidt, Few-Body Systems **55**(12), 1185 (2014), ISSN 0177-7963, <http://dx.doi.org/10.1007/s00601-014-0907-2>
168. D. Wilson, I. Cloët, L. Chang, C. Roberts, Phys.Rev. **C85**, 025205 (2012), 1112.2212
169. J. Segovia, C. Chen, I.C. Cloët, C.D. Roberts, S.M. Schmidt *et al.*, Few Body Syst. **55**, 1 (2014), 1308.5225
170. A.V. Efremov, A.V. Radyushkin, Phys. Lett. B **94**, 245 (1980)
171. A.V. Belitsky, X.D. Ji, F. Yuan, Phys. Rev. Lett. **91**, 092003 (2003)
172. S.J. Brodsky, J.R. Hiller, D.S. Hwang, V.A. Karmanov, Phys. Rev. D **69**, 076001 (2004)
173. A.F. Sill *et al.*, Phys. Rev. D **48**, 29 (1993)
174. M. Guidal, M.V. Polyakov, A.V. Radyushkin, M. Vanderhaeghen, Phys. Rev. D **72**, 054013 (2005)
175. V.A. Nesterenko, A.V. Radyushkin, Phys. Lett. B **128**, 439 (1983)
176. R.P. Feynman, *Photon-Hadron Interactions* (Benjamin, Reading, MA, 1972)

177. J. Bolz, R. Jakob, P. Kroll, M. Bergmann, N.G. Stefanis, *Z. Phys. C* **66**, 267 (1995)
178. P. Kroll, M. Schürmann, W. Schweiger, *Z. Phys. A* **338**, 339 (1991)
179. V.M. Braun, A. Lenz, M. Wittmann, *Phys. Rev. D* **73**, 076001 (2006)
180. X.D. Ji, J. Osborne, *Phys. Rev. D* **58**, 094018 (1998)
181. J.C. Collins, A. Freund, *Phys. Rev. D* **59**, 074009 (1999)
182. A.V. Radyushkin, *Phys. Rev. D* **58**, 114008 (1998)
183. D. Müller, D. Robaschik, B. Geyer, F.M. Dittes, J. Horejsi, *Fortsch. Phys.* **42**, 101 (1994)
184. X.D. Ji, *Phys. Rev. Lett.* **78**, 610 (1997)
185. A.V. Radyushkin, *Phys. Lett. B* **380**, 417 (1996)
186. X.D. Ji, *J. Phys. G* **24**, 1181 (1998)
187. K. Goeke, M.V. Polyakov, M. Vanderhaeghen, *Prog. Part. Nucl. Phys.* **47**, 401 (2001)
188. D. M., *Phys. Rept.* **388**, 41 (2003)
189. A.V. Belitsky, A.V. Radyushkin, *Phys. Rept.* **418**, 1 (2005)
190. X.D. Ji, *Ann. Rev. Nucl. Part. Sci.* **54**, 413 (2004)
191. M. Diehl, T. Feldmann, R. Jakob, P. Kroll, *Eur. Phys. J. C* **39**, 1 (2005)
192. M. Burkardt, *Int. J. Mod. Phys. A* **18**, 173 (2003)
193. M. Burkardt, *Phys. Lett. B* **595**, 245 (2004)
194. T. Janssens, R. Hofstadter, E.B. Hughes, M.R. Yearian, *Phys. Rev.* **142**, 922 (1966)
195. E.J. Brash, A. Kozlov, S. Li, G.M. Huber, *Phys. Rev. C* **65**, 051001 (2002)
196. W. Xu *et al.*, *Phys. Rev. Lett.* **85**, 2900 (2000)
197. W. Xu *et al.*, *Phys. Rev. C* **67**, 012201 (2003)
198. H. Anklin *et al.*, *Phys. Rev. Lett.* **428**, 248 (1998)
199. A. Lung *et al.*, *Phys. Rev. Lett.* **70**, 718 (1993)
200. D. Glazier *et al.*, *Eur. Phys. J. A* **24**, 101 (2005)
201. E. Brash, M. Jones, C. Perdrisat, V. Punjabi *et al.*, *JLab proposal* **04-108** (2004)
202. P. Hägler, *Phys. Rept.* **490**, 49 (2010), 0912.5483
203. C. Alexandrou, M. Constantinou, S. Dinter, V. Drach, K. Jansen *et al.*, *Phys. Rev.* **D88**(1), 014509 (2013), 1303.5979
204. T. Bhattacharya, S.D. Cohen, R. Gupta, A. Joseph, H.W. Lin *et al.*, *Phys. Rev.* **D89**, 094502 (2014), 1306.5435
205. J. Green, J. Negele, A. Pochinsky, S. Syritsyn, M. Engelhardt *et al.* (2014), 1404.4029
206. W. Alberico, S. Bilenky, C. Giunti, K. Graczyk, *Phys. Rev.* **C79**, 065204 (2009), 0812.3539
207. G. de Divitiis, R. Petronzio, N. Tantalo, *Phys. Lett.* **B718**, 589 (2012), 1208.5914